

# Macroscopic quantum tunneling in Josephson junctions -

a method to characterise a well-shielded low temperature setup

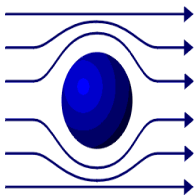
Georg Wild

Diploma Thesis



Advisor: Prof. Dr. R. Gross

2004



*Walther-Meissner-Institut*  
*Bayerische Akademie der Wissenschaften*  
*Walther-Meissner-Str. 8*  
*85748 Garching, GERMANY*









# CONTENTS

<i>Part I Introduction</i>	1
<i>Part II Theory</i>	5
1. <i>The classical theory of Josephson junctions</i>	9
1.1 Macroscopic Cooper-pair wave function	9
1.2 The gauge invariant phase difference	9
1.3 The Josephson effect	10
1.3.1 The first Josephson equation	11
1.3.2 The second Josephson relation	12
1.4 RCSJ-Model	13
2. <i>Josephson junction dynamics</i>	15
2.1 The basics	15
2.1.1 Overdamped junctions ( $Q \ll 1$ )	16
2.1.2 Underdamped junctions ( $Q \gg 1$ )	16
2.2 The classical Kramers' theory	17
2.2.1 Transition state theory	17
2.2.2 Kramers' theory	18
2.2.3 Kramers' theory in Josephson junctions	19
2.3 The quantum Kramers' theory and macroscopic quantum tunneling	21
2.3.1 Quantum tunneling in the presence of dissipation	21
2.4 The crossover regime	23
2.5 Discrete energy spectrum	25
2.6 Influence of microwaves and fluctuations	26
2.6.1 Resonant absorption of small microwave signals	26
3. <i>Quantum Computing</i>	29
3.1 Quantum bits	29
3.2 Superconducting qubits	31
3.3 Persistent current qubit with three Josephson junctions	33
3.3.1 The Hamiltonian	33
3.3.2 The Bloch functions	35
3.3.3 Center of mass system	35

---

3.3.4	Solution of the Schrödinger equation at $f=\frac{1}{2}$ — The tight binding model . . . . .	35
3.3.5	The coupling matrix element $t$ . . . . .	36
3.4	The DiVincenzo criterias and superconducting qubits . . . . .	37
 <i>Part III Experiments</i>		 39
4.	<i>Experimental setup</i> . . . . .	41
4.1	Dilution refrigerator and low temperature setup . . . . .	42
4.1.1	Temperature readout and sample heating . . . . .	43
4.2	Sample stage . . . . .	46
4.2.1	Overview . . . . .	46
4.2.2	Sputtering contacts and sample mounting . . . . .	47
4.3	Wiring and filtering stages . . . . .	48
4.3.1	Thermal anchoring . . . . .	49
4.4	Filters and current dividers . . . . .	50
4.4.1	The warm LCR filters . . . . .	50
4.4.2	RC filters and current dividers . . . . .	53
4.4.3	Copper-in-powder filters . . . . .	54
5.	<i>Experiments and results</i> . . . . .	57
5.1	<i>I-V-Characteristics</i> . . . . .	58
5.2	Escape rate measurements . . . . .	60
5.2.1	Measurement setup . . . . .	60
5.2.2	Data evaluation . . . . .	62
5.2.3	Discussion of results . . . . .	67
 <i>Part IV Summary</i>		 71

## ABSTRACT

Superconducting circuits based on Josephson junctions are very promising candidates for quantum bits which are the fundamental elements of a quantum computer. An essential requirement for realising a quantum computer are sufficiently long coherence times of the underlying qubits. To ensure that the intrinsic coherence times of the qubits are correctly determined the experimental environment must not contribute to the loss of coherence. In this work a low temperature setup was established to characterise Josephson junction devices in a highly shielded environment. To validate the setup with several stages of filtering against environmental electromagnetic noise and high frequency radiation the escape of individual Josephson junctions from the superconducting into the voltage state was investigated. The histograms of the currents where this switching takes place clearly showed a negligible amount of noise contributions with an accuracy below a fraction of a microamp. Furthermore, a crossover from thermally activated escape to a regime where the junction behavior is governed by Macroscopic Quantum Tunneling (MQT) has been observed in the experiments.



## ACKNOWLEDGEMENTS

During my last year at the WMI I have learned to appreciate the lifework of the former directors of the WMI. Making the WMI independent from the universities Walther Meissner and his successors founded an institute where people developed a cooperative spirit not only between people working on the same research project, but also in the whole institute. First of all I want to thank everybody for providing me this friendly environment.

I am thankful to the director of the WMI, Prof. Dr. R. Gross, for providing me the opportunity to take part in the research on solid state based quantum information processing and for supervising this work. I furthermore want to thank Dr. A. Marx for his time teaching me the physics of Josephson junctions and his help to get my experiments running. For building the dilution unit and running it I am indebted to Dr. C. Probst. His comprehensive experience in cryogenics was essential to get this results. I gratefully acknowledge the work done by our PhD students C. Coppi and M. Mariantoni. My successor as diploma student K. Madek helped me taking the actual measurements. E. Menzel wrote the labview programs in his practical course in our lab.

I enjoyed very much the team work with the diploma student H. Knoglinger. He was responsible for developing the junction technology, and prepared for me the samples even far into the night if necessary. The niobium Josephson junction and their characterisation was provided by T. Bauch from Chalmers University of Technology in Sweden.

But not only scientists are essential to get excellent results. So I will exceptionally thank the technicians helping to realise this work. The engineer T. Brenninger to take care of the sample stage drawings, the engineer W. Hehn to organise the dewar, G. Görblich to make the PCBs and the electronic technicians D. Guratzsch, U. Guggenberger and J. Hoess to help me with the circuits and the staff of the workshops.

This work was funded by the DFG (German science foundation) in the Cooperative Research Center 631 for Solid State Based Quantum Information Processing and by the Bavarian Academy of Sciences and Humanities.



## Part I

### INTRODUCTION



---

Today's electronic data processing systems are driven by transistor-based boolean (logic) gates packed on silicon chips, so called integrated circuits (ICs). In 1965 G.E. Moore predicted that the number of such gates on one IC will increase exponentially.<sup>27</sup> This prediction has proven to be valid up to now, reaching many millions of transistors per IC together with steadily increasing clock frequencies.

But obviously, this exponential growth cannot hold forever! On the one hand, enormous power dissipation rises the problem of cooling while, on the other hand, the elementary charge quantum limits the lowest possible current into the transistors. At least one electron is needed in capacitors to store information.

Amazingly, while charge quantisation poses a problem in conventional computing, the quantum nature opens new possibilities to do computations on a more advanced level based on quantum information theory, which is not speeding up conventional algorithms, but opens a fundamentally new approach to parallelise calculations. Thereby a coherent superposition of quantum states —not even measurable (hidden by quantum theory)— is processed in quantum gates.

But these are future dreams. Although some recent NMR experiments<sup>37</sup>, where the number 15 has been factorised by the quantum Shor algorithm, indicate the principal feasibility, the transition to solid-state systems, which opens the possibility to scale up a system, is not managed yet. Thus the DFG (German science foundation) started a cooperative research centre in Munich to find promising candidates for solid-state based quantum information processing systems. This work has been conducted within the scope of this research initiative.

The elementary unit of quantum computation is a quantum bit or qubit. A crucial issue for quantum computation is to get long enough coherence times of the qubits. Due to the energy gap superconducting devices are favourable in terms of decoherence and thermal excitation of states. For realising a superconducting qubit either the charge or current degree of freedom can be used.

The purpose of this work was to develop an experimental setup capable to measure persistent current qubits. This implies building and testing a setup operating in the millikelvin regime with electrical connections which are extremely well shielded from electromagnetic radiation.

A very elegant option to test the shielding against electromagnetic radiation is to measure the escape of Josephson junctions out of the superconducting state into the voltage state. A commonly used way to realise such experiments is to ramp up a current until the junction jumps out of the zero voltage state and to record a histogram of the switching currents ("ramping experiments"). These histograms are highly susceptible to external noise and radiation. The width of these histograms is, on the one hand, due to thermal effects (see section 2.2) and, on the other hand, due to quantum effects (see section 2.3).

Finding an outstanding theoretical feature (a quantum effect of a macroscopic degree of freedom) — the macroscopic quantum tunneling (MQT) — proves the negligibility of noise and radiation corresponding to fractions of the relevant critical current.

In the following theoretical part **II** I will give a short introduction into the classical theory of Josephson junctions (chapter **1**) and their dynamic properties (chapter **2**) and will elucidate the basics of quantum computing with persistent current qubits (chapter **3**). In chapter **4** I will describe the experimental setup while chapter **5** discusses the measurements and results. Part **IV** summarises the work.

Part II

THEORY



Classically, we distinguish two major groups of superconducting weak links. There are, on the one hand, the so called Josephson tunnel junctions –two superconductors separated by an insulating barrier– and, on the other hand, weak links –two superconductors weakly coupled by a non-superconducting metal. The weak links comprise point and blob type contacts, microbridges and sandwich structures with weakly conducting materials, whose Josephson properties are caused by the proximity effect<sup>6</sup>. Cooper-pairs penetrate into the non-superconducting interface causing a supercurrent through the link material.<sup>21</sup>

In contrast, the physical properties of Josephson tunnel junctions —which are the subject of this work— are due to a potential barrier between two superconductors and the quantum mechanical tunneling process. After a short introduction to the macroscopic wave function in superconductors (1.1) and the phase difference between two superconductors across a barrier (1.2) I will discuss the Josephson theory (1.3) and the Stewart-McCumber model (1.4).



## Chapter 1

### THE CLASSICAL THEORY OF JOSEPHSON JUNCTIONS

#### 1.1 Macroscopic Cooper-pair wave function

An important step towards a theoretical understanding of superconductivity in metals was the discovery of the isotope effect. The fact that the critical temperature of a superconductor scales inversely proportional to the square root of its atomic mass pointed out the involvement of electron-phonon-interaction in the mechanism of superconductivity and lead to the famous BCS theory<sup>2</sup>.

This theory states that in a superconductor in the ground state two electrons with opposite spin condensate into so called Cooper-pairs and the net momenta  $q = k_{\uparrow} + k_{\downarrow}$  of all these pairs are equal. Thus, we have to deal with a non-local phenomenon. A characteristic length scale is the coherence length  $\xi_0$ . Already the original BCS-work<sup>2</sup> approximated  $\xi_0 \sim \frac{1}{\delta k} \sim 10^{-4}$  cm assuming that the relevant vectors in k-space are of the order  $\delta k \sim \frac{k_B T_c}{E_F} k_F \sim 10^4$  cm<sup>-1</sup>.

Therefore, we have to deal with macroscopic center of mass wave functions for the superconducting electrodes on both sides of the Josephson junction.

#### 1.2 The gauge invariant phase difference

In quantum mechanics physical quantities are represented by Hermitian operators. Their non-ambiguous eigenvalues define the expectation value of the observables  $\hat{O}$

$$\langle \hat{O} \rangle = \langle \psi | \hat{O} | \psi \rangle = \int \psi^* \hat{O} \psi d^3x \quad .$$

Being locally gauge invariant electromagnetic field theory cannot provide a defined phase angle  $\phi_1$  and  $\phi_2$  for both superconducting electrodes simultaneously in a junction, not even the phase difference is unambiguously defined.

Therefore, the phase difference of the wave functions on both sides of the barrier in Josephson junctions is no observable. Thus, this quantity cannot define the current through a junction. Obviously, a gauge invariant phase difference, can be derived integrating the canonical momentum  $\vec{k}$  along a path from a point in superconductor 1 to a

point in superconductor 2

$$\begin{aligned}\varphi &= \int_1^2 \vec{k} d\vec{r} = \int_1^2 (\vec{p} - e\vec{A}) d\vec{r} \\ &= \phi_2 - \phi_1 - \frac{2\pi}{\phi_0} \int_1^2 \vec{A} d\vec{r}\end{aligned}\quad (1.1)$$

where  $\phi_0 = 2.068 \cdot 10^{-15}$  Wb is the flux quantum. We will see in the next section that there is a simple relation between  $\varphi$  and the voltage across a junction.<sup>33</sup>

### 1.3 The Josephson effect

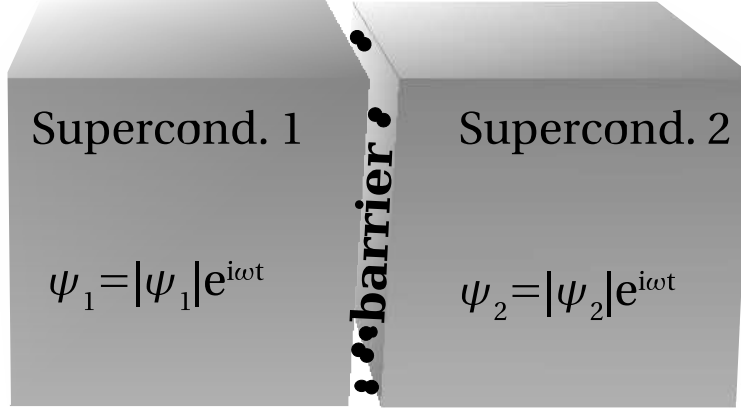


**Figure 1.1:** Cooper-pairs tunneling through a thin barrier between two superconductors.

The theory of Cooper-pair tunneling through thin barriers between two superconductors was developed in the sixties of the last century. B. D. Josephson realised that the probability of a Cooper-pair tunneling through a barrier is not negligible compared to one electron tunneling because it is a coherent process. He used Bogoliubov-theory, which approximates the physics of superconductivity in second quantisation.<sup>16</sup> In the following I will explain the theory in a less theoretical manner.

I will only treat the one-dimensional case with  $x$  representing the coordinate perpendicular to the barrier plane. Furthermore, I focus on lumped junctions where the current through the barrier is spatially homogeneous.  $\phi$  will always denote the phase of the macroscopic wave function in the superconducting electrode, whereas  $\varphi$  defines the gauge-invariant phase difference between two superconductors (c.f. equation (1.1)).

## 1.3.1 The first Josephson equation

By sending a current smaller than the so called critical current  $I_c$  through a Josephson junction no voltage drop will be observed — it remains in the zero voltage state. This so called dc- or first Josephson effect can be described using the weak coupling approximation. Here one assumes a barrier between two superconductors with the ground state energy levels  $E_1$  and  $E_2$  and the macroscopic wave functions  $\psi_1$  and  $\psi_2$ . Thus in the uncoupled limit the Schrödinger equation reads

$$\begin{pmatrix} E_1 & \\ & E_2 \end{pmatrix} \begin{pmatrix} \psi_1 \\ \psi_2 \end{pmatrix} \equiv \vec{E} \vec{\psi} = \overleftarrow{H} \vec{\psi} = i\hbar \frac{\partial}{\partial t} \begin{pmatrix} \psi_1 \\ \psi_2 \end{pmatrix} \equiv i\hbar \dot{\vec{\psi}} \quad .$$

For thin barriers Cooper-pairs can tunnel through and thereby couple the wave functions of both superconductors. This can be expressed by adding a coupling term  $\overleftarrow{H}_t = \begin{pmatrix} 0 & K \\ K & 0 \end{pmatrix}$  to the Hamiltonian

$$\left( \overleftarrow{H} + \overleftarrow{H}_t \right) \vec{\psi} = i\hbar \dot{\vec{\psi}} \quad .$$

Using  $\psi_1 = \sqrt{n_1} e^{i\phi_1}$  and  $\psi_2 = \sqrt{n_2} e^{i\phi_2}$  with  $n_1, n_2$  the Cooper-pair densities one has to solve the linear differential equation system

$$\frac{\dot{n}_1 e^{i\phi_1}}{2\sqrt{n_1}} + i\sqrt{n_1} e^{i\phi_1} \dot{\phi}_1 = -\frac{i}{\hbar} \left( E_1 \sqrt{n_1} e^{i\phi_1} + K \sqrt{n_2} e^{i\phi_2} \right) \quad (1.2)$$

$$\frac{\dot{n}_2 e^{i\phi_2}}{2\sqrt{n_2}} + i\sqrt{n_2} e^{i\phi_2} \dot{\phi}_2 = -\frac{i}{\hbar} \left( E_2 \sqrt{n_2} e^{i\phi_2} + K \sqrt{n_1} e^{i\phi_1} \right) \quad . \quad (1.3)$$

Separating into real and imaginary parts one gets<sup>13</sup> for the real part (assuming identical superconductors  $n_1 = n_2 = n$ )

$$\dot{n}_1 = \frac{2K}{\hbar} n \sin(\phi_2 - \phi_1) = -\dot{n}_2 \quad .$$

Thus there is a Cooper-pair current from one superconductor into the other. The magnitude of the current is proportional to the sine of the phase difference across the barrier

$$I = I_c \sin(\phi_2 - \phi_1) \quad . \quad (1.4)$$

This simple theory predicts the critical current

$$I_c = \frac{2K(2e)}{\hbar} V n$$

proportional to the volume of one superconducting electrode  $V$ , the charge of a Cooper-pair  $2e$  with the elementary charge quantum  $e = 1.602 \cdot 10^{-19}$  C, the Cooper-pair

density  $n$  in one superconducting electrode and the coupling constant  $K$ .  $\hbar = h/2\pi = 1.055 \cdot 10^{-34}$  Js denotes the reduced Planck constant. In more complex theories the expression for the critical current depends on the junction geometry and electrode materials and thus on the superconducting energy gap of both electrodes, the junction normal resistance and the temperature.<sup>1, 21</sup>

### 1.3.2 The second Josephson relation

Currents above the critical current  $I_c$  cannot be carried by Cooper-pairs exclusively. Therefore, the junction switches from the zero voltage state to a finite voltage state (running state). The mathematical treatment can be handled with the imaginary part of equations (1.2) and (1.3)

$$\begin{aligned} i\sqrt{n}\dot{\phi}_1 &= -\frac{i}{\hbar} (E_1\sqrt{n} + K\sqrt{n}\cos(\phi_2 - \phi_1)) \\ i\sqrt{n}\dot{\phi}_2 &= -\frac{i}{\hbar} (E_2\sqrt{n} + K\sqrt{n}\cos(\phi_1 - \phi_2)) \end{aligned} .$$

Subtracting these equations results in the second or ac Josephson equation

$$\hbar\dot{\phi} = (E_1 - E_2) \equiv (2e)U \quad (1.5)$$

where  $U$  is the potential difference across the barrier.

Thus at a constant applied voltage the phase difference across a Josephson junction and therefore the supercurrent through it is oscillating with a constant frequency. An applied voltage of  $1 \mu\text{V}$  equals a frequency of 483.6 MHz. Because of the better measurability of frequencies this can be used as a voltage reference.

## 1.4 RCSJ-Model

A model capable of describing real Josephson junctions should take into account the capacitance between the two superconductors on both sides of the thin barrier. At finite temperatures, thermally excited quasiparticles in the electrodes can tunnel through the barrier causing the quasiparticle resistance  $R$ . To describe these effects, in 1965 the Stewart-McCumber model was developed.<sup>26, 32</sup> It models a Josephson junction as a parallel connection of an ideal Josephson element, a capacitance  $C$  and a voltage independent normal resistance  $R$  depicted in fig. 1.2 leading to a total bias current  $I_b = I_c \sin \varphi + \frac{U}{R} + C\dot{U}$  through the structure. This model is called the **R**esistively and **C**apacitatively **S**hunted **J**unction (RCSJ) model. Using the second Josephson equation (1.5)

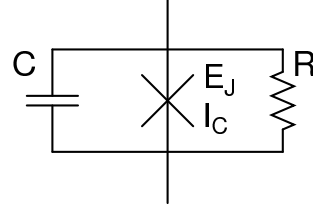


Figure 1.2: RCSJ-Model

$$I_b = I_c \sin \varphi + \frac{1}{R} \left( \frac{\phi_0}{2\pi} \right) \frac{\partial \varphi}{\partial t} + C \left( \frac{\phi_0}{2\pi} \right) \frac{\partial^2 \varphi}{\partial t^2} \quad (1.6)$$

is obtained, where  $\phi_0 = 2.068 \times 10^{-15}$  Wb is the flux quantum. Introducing a “tilted washboard potential”

$$U(I_b, \varphi) = - \left( \frac{\phi_0}{2\pi} \right) I_b \varphi - \underbrace{\frac{\phi_0}{2\pi} I_c}_{E_J} \cos \varphi = -E_J \left( \frac{I_b}{I_c} \varphi + \cos \varphi \right) \quad , \quad (1.7)$$

equation (1.6) can be rewritten in the form

$$C \left( \frac{\phi_0}{2\pi} \right)^2 \frac{\partial^2 \varphi}{\partial t^2} + \frac{1}{R} \left( \frac{\phi_0}{2\pi} \right)^2 \frac{\partial \varphi}{\partial t} + \frac{d}{d\varphi} \left[ \overbrace{-E_J \left( \frac{I_b}{I_c} \varphi + \cos \varphi \right)}^{U(I_b, \varphi)} \right] = 0 \quad . \quad (1.8)$$

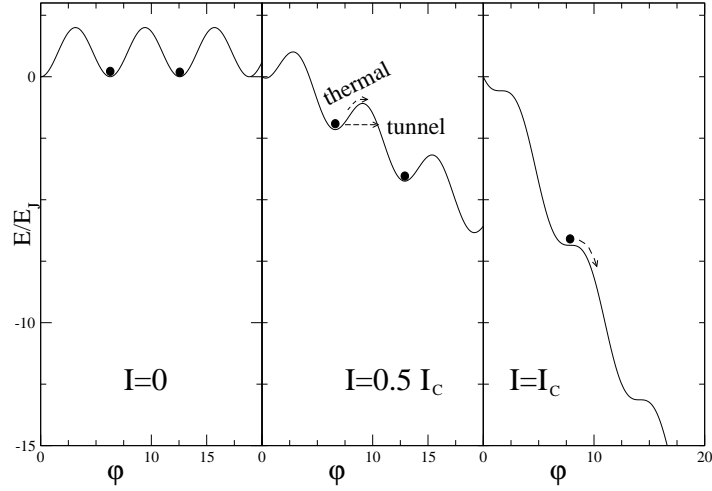


**Figure 1.3:** Tilted washboard potential

Thus a RCSJ circuit is equivalent to a classical particle with a mass proportional to the capacitance of the circuit ( $M = C(\phi_0/2\pi)^2$ ) and moving with ohmic dissipation proportional to the normal conductance ( $\gamma = \frac{1}{R}(\phi_0/2\pi)^2$ ) in a tilted washboard potential. Introducing the zero-current plasma frequency

$$\omega_{p0} = \sqrt{\frac{2eI_c}{\hbar C}} = \sqrt{\frac{2\pi I_c}{\phi_0 C}} \quad (1.9)$$

allows to transform the time to the dimensionless variable  $\tau = \omega_{p0}t$  and to arrive at a compact version of equation (1.8)

$$\frac{d^2\varphi}{d\tau^2} + Q^{-1}\frac{d\varphi}{d\tau} + \sin\varphi = \frac{I_b}{I_c} \quad (1.10)$$

Here,  $Q = \omega_p RC$  denotes the quality factor, which is the parameter characterising the damping. As we will see later, a hysteresis in the current-voltage characteristics of a junction emerges for  $Q$  values exceeding a specific value. Also widely used is the Stewart-McCumber-parameter  $\beta_c = Q^2$ .<sup>33</sup>

Adding a fluctuating current  $I_F(t)$ , whose source may be thermal noise in dissipative elements and other external perturbations, to equation (1.6)

$$I_b = I_c \sin\varphi + \frac{1}{R} \left( \frac{\phi_0}{2\pi} \right) \frac{\partial\varphi}{\partial t} + C \left( \frac{\phi_0}{2\pi} \right) \frac{\partial^2\varphi}{\partial t^2} + I_F(t)$$

results in a modification of the tilted washboard potential

$$U(I, \varphi) = -E_J \left( \frac{I - I_F(t)}{I_c} \varphi + \cos\varphi \right), \quad (1.11)$$

i. e. the fluctuation current will also have a strong influence on the switching dynamics to the voltage state (“escape behavior”).

## Chapter 2

### JOSEPHSON JUNCTION DYNAMICS

#### 2.1 The basics

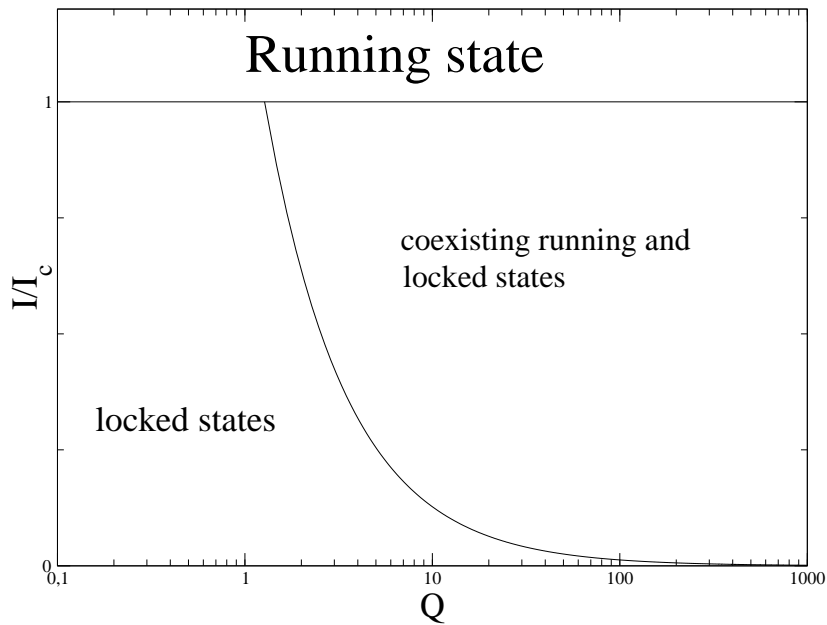


**Figure 2.1:** Phase diagram of a Josephson junction in the RCSJ model.

As described in the previous section Josephson junctions can be described as particles moving in a tilted washboard potential. In such a potential metastable states exist. Depending on the junction quality factor  $Q$  and the bias current  $I_b$  the junction can be in the voltage state or in the superconducting state, or –in the picture of the model– the particle can be trapped in a metastable state or has enough kinetic energy to get over the barriers.

If the bias current is exceeding the critical current, the barriers are washed out by the tilting of the potential and the junction is inevitably in the running state. The phase continually increases ( $\frac{d\varphi}{dt} > 0$ ) inducing a voltage over the junction due to the second Josephson equation (1.5). On the other hand, if no bias current is applied, the potential is not tilted and there are degenerate stable ground states. In this case the phase

remains constant ( $\varphi = \arcsin \frac{I_b}{I_c}$ ) and no voltage drops across the junction. Finite bias currents below the critical current are more complicated to treat. Although overdamped junctions ( $Q \ll 1$ ) can be treated relatively simply, underdamped junctions ( $Q \gg 1$ ) need to be considered more carefully due to hysteretic effects.<sup>33</sup> The dynamic properties of junctions can be visualized in the phase diagram shown in fig. 2.1. Here, three phases are depicted –running state, locked states, and coexisting running and locked states.

### 2.1.1 Overdamped junctions ( $Q \ll 1$ )

In this case looking at the tilted washboard potential one realises that viscous damping dominates inertia. Therefore, no hysteresis exists in these junctions. Thus, due to their pronounced switching underdamped junctions are more appropriate for ramping experiments.

### 2.1.2 Underdamped junctions ( $Q \gg 1$ )

Underdamped junctions strongly differ from overdamped junctions because they show hysteresis. Continually increasing the bias current  $I_b$  from zero, the junction jumps discontinuously into the running state at the critical current  $I_c$ , where the gauge-invariant phase difference suddenly starts to increase at a rate of  $\frac{d\varphi}{dt} = \frac{2e}{\hbar} V$ . Thus, after leaving the zero voltage state the junction suddenly switches to a finite voltage  $V = RI_c$ . In contrast, at this transition BCS-theory predicts a voltage jump of  $V = \frac{2\Delta}{e}$ , where  $\Delta$  is the superconductor's energy gap. For higher currents a linear dependence  $V = I_b \cdot R$  is obtained (for the underdamped case, too).

A significant difference appears for decreasing the bias current. While an overdamped junction switches back into the zero voltage state at the critical current  $I_c$ , an underdamped junction does not switch back to zero before the retrapping current  $I_r < I_c$  is reached. This current can be estimated<sup>33</sup>

$$I_r \approx \frac{4 I_c}{\pi Q} . \quad (2.1)$$

This can be illustrated with the particle in the tilted washboard potential model: After crossing the potential wall and falling to the next local potential minimum, the particle has accumulated enough kinetic energy to overcome even the next potential. That is, to stop the falling particle one needs to decrease the potential tilt, which is achieved by a lower bias current.

Equation (1.11) shows that the fluctuating current wobbles the tilted potential. This causes premature switching and retrapping at higher currents, respectively, in underdamped junctions. Especially in ramping experiments the histogram of escape currents shifts to lower currents and becomes broader.

## 2.2 The classical Kramers' theory

Kramers' theory describes a classical particle of mass  $m$  moving in a one-dimensional asymmetric double-well potential  $U(x)$ . This problem was intensively studied theoretically, obviously as reaction-rate-theory in chemistry and of course in physics. The original work of Kramers<sup>18</sup> treated almost all limits, so only minor improvements have been added in later publications.

In our case, where we want to describe the escape probability per time interval from the zero voltage state into the voltage state ("escape rate") in underdamped Josephson junctions with this theory, we can use the transition probability from one well into the other given by Kramers' theory and neglect the back-flow.

In this section I will give a short introduction to transition state theory (section 2.2.1), summarise the results of Kramers' theory (section 2.2.2) and apply this theory to underdamped Josephson junctions (section 2.2.3).

### 2.2.1 Transition state theory

The transition-state-theory (TST) is a classical approach to treat the escape from a metastable state.<sup>15</sup> Let us assume a particle in the tilted potential shown in fig. 2.2 with a metastable state at point  $x = a$ . The bottleneck for the particle leaving the metastable state is immediately observable at the top of the barrier of height  $W$  at  $x = b$ . Before using Kramers' theory to describe this problem, let me first explain it with the less complex transition-state ansatz.

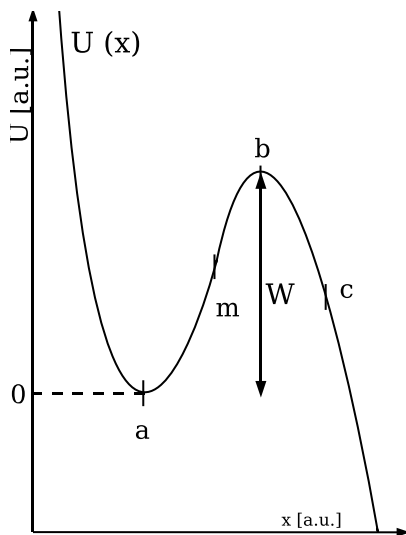


**Figure 2.2:** Potential with a metastable state at  $x=a$ . [36]

the Boltzmann weighting function at a given temperature  $T$  to calculate the escape rate from the metastable state. This theory always overestimates the escape rate such that the real escape rate  $\Gamma$  is always smaller than the calculated rate  $\Gamma_{TST}$ . In our case, the

The transition-state ansatz uses two key assumptions, namely the strong-coupling assumption and the point of no return  $c$ . The strong-coupling assumption requires a system in thermal equilibrium, or equivalently speaking, the timescale for the particle to escape out of the metastable state must be much longer than the time necessary for thermalization inside the metastable state. The point of no return assumption states that any orbit crossing a certain point  $c$  on the outer side of the well will not recross it. This means, that a particle that has overcome the potential will not move back into the metastable state. In the following I will use these assumptions to define a theory in the classical limit neglecting the probability of tunneling through the barrier. I will use the canonical TST, which uses

Boltzmann factor helps to minimise the phase space at the top of the barrier. Thus I will define the point of no return at  $c = b$ , which gives little overestimation.

To treat our limit let me use the “flux-over-population” method. This method looks for a stationary solution using the assumption that particles are injected by a source into the metastable region of attraction and removed by a sink on the other side of the barrier. In this way one can apply a stationary probability distribution function for the particle’s position, which can be easily calculated with statistics. Particles overcoming the barrier are removed such that this function is zero for  $x > b$ .

With these assumptions the probability  $P_{out}$  that a particle leaves the metastable state is given by<sup>4</sup>

$$\begin{aligned} P_{out} &\approx \int_0^\infty dv \int_{b-v\Delta t}^b dx \frac{e^{-\frac{mv^2}{2k_B T}}}{\int_{-\infty}^\infty dv' e^{-\frac{mv'^2}{2k_B T}}} \frac{e^{-\frac{U(b)}{k_B T}}}{\int_{-\infty}^\infty dx' e^{-\frac{U(x')}{k_B T}}} \\ &\approx \Delta t \sqrt{\frac{k_B T}{2\pi m}} \left( \int_{-\infty}^b dx e^{-\frac{U(x)-U(a)}{k_B T}} \right)^{-1} e^{-\frac{W}{k_B T}} . \end{aligned} \quad (2.2)$$

where  $k_B = 1.38 \cdot 10^{-23} \text{J/K}$  denotes the Boltzmann constant and  $\Delta t$  is a time interval. If the energy is sufficiently low we can use a harmonic approximation for the potential around  $x = a$

$$\tilde{U}(x) = U(a) + \frac{1}{2} m \omega_a^2 (x - a)^2 + o((x - a)^3)$$

for the potential around the metastable minimum where the attempt frequency  $\omega_a$  denotes the frequency of small oscillations around the potential minimum. Approximating the integration limits in equation (2.2) with  $\pm\infty$  results in the transition state escape rate

$$\Gamma_{TST} = \frac{\omega_a}{2\pi} e^{-W/k_B T} . \quad (2.3)$$

N. G. van Kampen points out an illustrative interpretation of this in his book.<sup>36</sup> A particle is oscillating with frequency  $\omega_a$  in a harmonic potential. Thus the “hit” or “attempt frequency” on the wall is  $\frac{\omega_a}{2\pi}$ . Every time the particle hits the wall it has the probability  $e^{-W/k_B T}$  to cross the wall.

### 2.2.2 Kramers’ theory

Kramers’ theory describes a classical particle of mass  $m$  moving in a one-dimensional asymmetric double-well potential  $U(x)$ . The remaining degrees of freedom acting on this particle are represented by a heat bath at temperature  $T$ , which is described by a Gaussian white noise fluctuating force  $\xi(t)$  obeying

$$\begin{aligned} \langle \xi(t) \rangle &= 0 && \text{and} \\ \langle \xi(t) \xi(s) \rangle &= 2m\gamma k_B T \delta(t - s) \end{aligned}$$

and a linear damping force  $-m\gamma\dot{x}$ , where  $\gamma$  denotes the damping constant. The equation of motion takes the form of the Langevin equation

$$m\ddot{x} = -\frac{\partial U(x)}{\partial x} - \gamma m\dot{x} + \xi(t) \quad . \quad (2.4)$$

The dynamics of this two-dimensional system with the dimensions position  $x$  and velocity  $v = \dot{x}$  can be described by the Klein-Kramers equation

$$\frac{\partial p(x, v, t)}{\partial t} = \left( -\frac{\partial}{\partial x} v + \frac{\partial}{\partial v} \frac{U'(x) + m\gamma v}{m} + \frac{\gamma k_B T}{m} \frac{\partial^2}{\partial v^2} \right) p(x, v, t) \quad , \quad (2.5)$$

where  $U'(x)$  denotes the spatial deviation of  $U(x)$ .<sup>15, 18</sup>

Now in our case we want to treat the escape of a particle from a metastable state over a potential barrier. Here, we do not have a double-well potential, but our case can be simply deduced from Kramers' problem by only allowing transitions out of the metastable state.

For our RCSJ potential we have to deal with extremely weak friction. In this limit the particle is exposed to very little damping and very little noise, and, as a result, the particle follows a unperturbed conservative equation of motion.<sup>15</sup> Then the energy, or equivalently speaking, the action  $I(E) = \oint p dq$  can be used to describe the dynamics of a particle. In this limit Kramers found for the escape rate

$$\Gamma = \frac{\gamma I(W)}{k_B T} \frac{\omega_a}{2\pi} \exp\left(-\frac{W}{k_B T}\right) \quad . \quad (2.6)$$

Therefore, he used the assumption that the phase space density vanishes at the top of the barrier. This leads to an inaccuracy in the limit of extremely weak damping, which is treated in this work. Therefore, in the thermal limit I will use an improved version of equation (2.6)

$$\Gamma = \frac{\sqrt{1 + \frac{4\alpha k_B T}{\gamma I(W)}} - 1}{\sqrt{1 + \frac{4\alpha k_B T}{\gamma I(W)}} + 1} \frac{\gamma I(W)}{k_B T} \frac{\omega_a}{2\pi} \exp\left(-\frac{W}{k_B T}\right) \quad (2.7)$$

developed by M. Büttiker et al.<sup>5</sup> The parameter  $\alpha$  gives a factor for phase space correction. There have been some efforts to calculate its value, but as far as I know there is still no consistency with experiment (see Ref. [25] and references therein). Therefore, one may treat  $\alpha$  as a free parameter, which should be slightly larger than one.

### 2.2.3 Application of Kramers' theory to underdamped Josephson junctions

As we have seen in section 1.4 the RCSJ model implies a tilted washboard potential. In the case  $I < I_c$  the sinusoidal part of the potential generates a sequence of metastable states with a period of  $2\pi$ . Hence, looking at one metastable state we can use Kramers'

theory to treat the escape over the corresponding single barrier. In underdamped junctions this is similar to bringing the junction into the running state. The barrier height in the RCSJ potential can be calculated to

$$\begin{aligned} W &= 2E_J \left( \sqrt{1 - i_b^2} - i_b \arccos i_b \right) & (I_b < I_c) \\ &\approx \frac{4\sqrt{2}}{3} E_J (1 - i_b)^{3/2} & (I_b \approx I_c) \end{aligned} \quad (2.8)$$

where the attempt frequency

$$\omega_a = \omega_{p0} (1 - i_b^2)^{1/4} \quad (2.9)$$

denotes the frequency of small oscillations around a potential minimum and  $i_b$  abbreviates the quotient  $\frac{I_b}{I_c}$ . The difference between  $\omega_a$  and  $\omega_{p0}$  from equation (1.9) is only significant for  $I_b \approx I_c$ . Using Kramers' low damping theory with Büttiker's improvement we get the escape rate<sup>25</sup>

$$\Gamma_t = a_t \frac{\omega_a}{2\pi} \exp\left(-\frac{W}{k_B T}\right) \quad (2.10)$$

with

$$a_t = \frac{4\alpha}{\left(\sqrt{1 + \frac{\alpha Q k_B T}{1.8 W}} + 1\right)^2} \quad (2.11)$$

$\alpha$  denotes the phase space correction factor mentioned in section 2.2.2. For Josephson junctions Martinis et al. fitted this factor for their experiments to  $1 \pm 0.05$ . I will use in the following this value because the quality of our measurements at higher temperatures is not good enough to get such a precise value.

With a more sophisticated design of shielding, the development of sensitive measurement techniques and the advance in low temperature technology it was possible to minimise parasitic effects and to reach very low temperatures ( $T \ll 100$  mK). In this temperature range a new path of escape opens—the so called macroscopic quantum tunneling—which I will treat in the next section. The classical treatment described above only deals with thermally activated escape, which does not rely on quantum tunneling.

### 2.3 The quantum Kramers' theory and macroscopic quantum tunneling

In nuclear physics the radioactive decay of a nucleus is explained by tunneling through a potential well. This potential is formed by a combination of the short-range strong interaction and the long range Coulomb interaction, giving a high barrier at the “nucleus border”.<sup>19</sup> A simple theory gives an escape rate  $\Gamma$  of e.g.  $\alpha$ -particles overcoming the atomic border via **Wenzel-Kramers-Brillouin** (WKB) approximation<sup>29</sup>

$$\Gamma \propto e^{-2G} \quad ,$$

where  $G$  denotes the Gamow factor

$$G(E_a) = \frac{1}{\hbar} \int_R^{R'} \sqrt{2m(U(R) - E_a)} dr \quad .$$

$E_a$  represents the energy of the escaping particle and  $R$  and  $R'$  are defined via

$$U \left( \begin{array}{c} R \\ R' \end{array} \right) = \left( \begin{array}{c} E_a \\ E_a \end{array} \right) \quad . \quad (2.12)$$

This simple picture is not applicable to our problem; we have to deal with quantum tunneling in the presence of dissipation.

#### 2.3.1 Quantum tunneling in the presence of dissipation

The treatment of this limit is more complicated than the classical limit of Kramers' theory. Therefore, different methods have been discussed to derive the rate of quantum tunneling at low temperatures. A widely used access to this problem is Feynman's functional integral formulation, but only few analytical solutions are known.

One example is a cubic potential  $U(x) = \frac{m}{2} \omega_0^2 x^2 \left(1 - \frac{x}{x_0}\right)$  with the free parameter  $x_0$  and strict ohmic weak dissipation.<sup>10, 15</sup> With the barrier height of the cubic potential

$$E_b = \frac{2m\omega_0^2 x_0^2}{27},$$

the escape rate

$$\Gamma_q = a_q(T) \exp(-S_B(T)) \quad (2.13)$$

can be derived. Approximate expressions for the parameters  $a_q(T)$  and  $S_B(T)$  in equation (2.13) (with friction coefficient  $\alpha \rightarrow 0$ ) are given by Freidkin et al.<sup>10</sup>

$$S_B(T) = \frac{36}{5} \frac{W}{\hbar\omega_0} \left[ 1 + \alpha \left( \frac{45\zeta(3)}{\pi^3} - \frac{5}{2\pi} \left( \frac{2\pi k_B T}{\hbar\omega_0} \right)^2 - \frac{\pi}{12} \left( \frac{2\pi k_B T}{\hbar\omega_0} \right)^4 + \dots \right) \right]$$

$$a_q(T=0) = 12\omega_0 \sqrt{\frac{3}{2\pi} \frac{W}{\hbar\omega_0}} \exp(2.860\alpha) \quad ,$$

where  $\zeta$  denotes Riemann's zeta function ( $\zeta(3) \approx 1.2021$ ).

The accuracy of these approximations can be estimated by comparing these results to numerical calculations. It turns out that the result for  $T < 0.6T_{cr} = 0.6\frac{\hbar\omega_a}{2\pi k_B}$  are acceptable. The validity range for the damping parameter  $\alpha$  is much smaller resulting in significantly questionable results for  $\alpha \gtrsim 0.1$ . In the RCSJ-model the cosine potential has to be approximated by a cubic potential to apply the above described solution. For Josephson junctions we arrive at<sup>25</sup>

$$\Gamma_q = a_q \left(\frac{\omega_a}{2\pi}\right) \exp\left(-\frac{36}{5} \frac{W}{\hbar\omega_a} \left(1 + 1.74 \frac{1}{2Q}\right)\right) \quad (2.14)$$

$$a_q = \sqrt{120\pi \left(\frac{7.2W}{\hbar\omega_a}\right)} \quad . \quad (2.15)$$

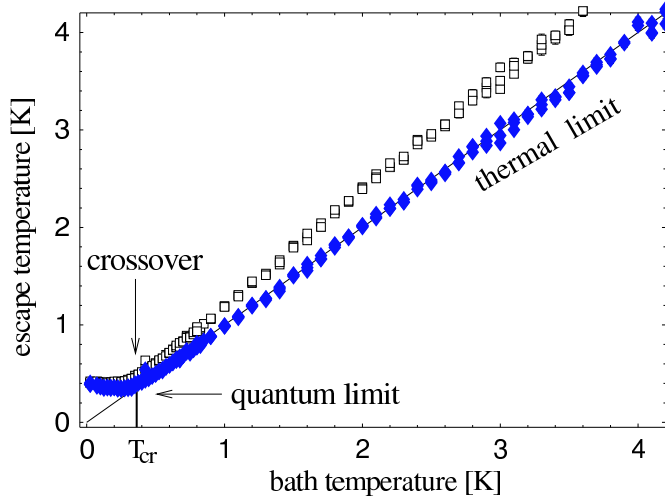


**Figure 2.3:** Escape temperature  $T_{esc}$  extracted from data in ref. [41]. The open symbols show the escape temperature extracted from the measurement using equation (2.16) while the solid symbols use equation (2.10) with the prefactor  $a_t$  defined in equation (2.11) to define a characteristic temperature.  $T_{cr}$  denotes the crossover temperature defined in equation (2.17).

## 2.4 The crossover regime

In the preceding sections 2.2 and 2.3 the thermal and the quantum limit of escape out of a metastable state have been discussed. In the intermediate range there should be a crossover between these two limiting cases. To discuss this transition Martinis et al.<sup>25</sup> introduced the escape temperature

$$\Gamma = \frac{\omega_a}{2\pi} e^{-\frac{W}{k_B T_{esc}}} \quad . \quad (2.16)$$

In the thermal limit the escape temperature

$$T_{esc} = \frac{T}{1 - p_t} \quad (k_B T \gg \hbar \omega_p)$$

is obtained, where

$$p_t = \frac{\ln a_t}{\frac{W}{k_B T}} \quad .$$

In the quantum limit the equations (2.13) and (2.16) reduce to

$$T_{esc} = \frac{\hbar \omega_a}{7.2 k_B} \frac{1}{1 + \frac{0.87}{Q}} \frac{1}{1 - p_q} \quad (T = 0) \quad ,$$

where

$$p_q = \frac{\ln a_q}{\frac{7.2W}{\hbar \omega_a} \left(1 + \frac{0.87}{Q}\right)} \quad .$$

Since the escape temperature is almost independent of the bias current (except for a weak bias current dependence via  $\omega_a$  and very high quality factors of the junction),  $T_{esc}$  is a well suited parameter to describe the phenomenon of escape out of a metastable state.

In fig. 2.3 we can see a measurement of the escape temperature vs. bath temperature. At the crossover temperature

$$T_{cr} = \frac{\hbar\omega_a}{2\pi k_B} \left( \sqrt{1 + \left(\frac{1}{2Q}\right)^2} - \frac{1}{2Q} \right)$$

we observe a crossover between the above limits.<sup>42</sup> For the Nb/Al<sub>2</sub>O<sub>3</sub>/Nb junction investigated in this work the quality factor is quite high ( $Q \approx 100$ ). Therefore, I will use the approximation formula

$$T_{cr} = \frac{\hbar\omega_a}{2\pi k_B} \tag{2.17}$$

for the crossover temperature.

## 2.5 Discrete energy spectrum

As explained above up to a critical tilt angle the tilted washboard potential induces metastable states. According to quantum mechanics localising the “phase”-particle leads to a discrete energy spectrum. This has already been experimentally observed by Martinis et al.<sup>24</sup>

To get a rough idea of the energy levels we apply for simplicity a harmonic approximation around a potential minimum (see fig. 2.4). Then the number of levels in the well can be estimated

$$N = \frac{W}{\hbar\omega_a} \quad (2.18)$$

with the discrete energy levels at

$$E_n = \frac{\hbar\omega_a}{2} \left( n + \frac{1}{2} \right) \quad (2.19)$$

where  $n$  is an arbitrary integer enumerating the ground state  $n = 0$  and the excited states  $n = 1 \dots N$ , and  $W$  is the barrier height defined in section 2.2.1.

The original cosine potential is anharmonic, but for currents slightly below  $I_c$  it is well approximated by the cubic potential.<sup>9</sup> For the following discussion we neglect the tunneling through the barrier. Then the boundary conditions for the eigenstates require that the eigenfunctions vanish outside the well. Obviously with higher excitation number  $n$  the waves fit better in the well and therefore the spacing of eigenenergies decreases with higher energy. The same argument can be used to discuss the dependence of the level separation on the bias current. Increasing the bias current would result in steeper borders of the potential. This impedes fitting whole waves in the potential resulting in a larger level separation. This can also be seen by looking at the current dependence of the plasma frequency.

The phase particle can be excited to higher energy levels by rapid change of bias current, thermal excitation and microwave radiation.<sup>22</sup> In the following I will elucidate the latter one.

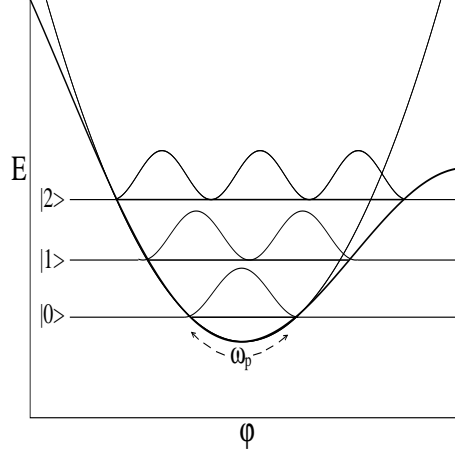


**Figure 2.4:** Discrete energy levels in the metastable states

## 2.6 Influence of microwaves and fluctuations

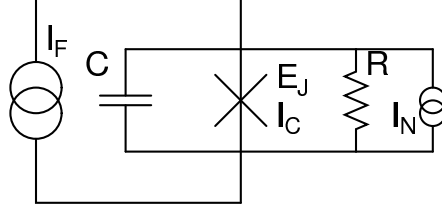


**Figure 2.5:** RCSJ-Model in the presence of fluctuations. Microwaves can be directly irradiated to the junction.

The behaviour of Josephson junctions under the influence of externally applied microwaves with amplitude  $I_{m0}$  and frequency  $\Omega$  can be modelled by adding an alternating driving current

$$I_m(t) = I_{m0} \sin(\Omega t + \varphi) \quad (2.20)$$

to the Steward-McCumber model. The noise spectral density of an additional thermal noise source  $I_N$  is<sup>7</sup>

$$S_{I_N} = \frac{2k_B T}{\pi R} \quad . \quad (2.21)$$

The effect of the noise is to wobble the potential in a random way resulting in premature switching of the junction to the voltage state.

Using Kirchhoff's laws the microwave driven system can be described by an equation similar to the one of a driven physical pendulum

$$C \left( \frac{\phi_0}{2\pi} \right)^2 \frac{\partial^2 \varphi}{\partial t^2} + \frac{1}{R} \left( \frac{\phi_0}{2\pi} \right)^2 \frac{\partial \varphi}{\partial t} + \frac{d}{d\varphi} \left[ -E_J \left( \frac{I}{I_C} \varphi + \cos \varphi \right) \right] = \frac{\phi_0}{2\pi} [I_N(t) + I_m(t)] \quad . \quad (2.22)$$

The term on the right hand side represents the pendulum's external driving force. To my knowledge no analytical solution of this problem is known yet. Here, I will only treat the limit of small microwave signals.

### 2.6.1 Resonant absorption of small microwave signals

By irradiating a Josephson junction with small amplitude microwave signals higher energy levels can be populated. To understand how this works let us have a closer look on the harmonic approximation again. To give a naive picture let us assume the microwaves being in resonance with the “phase particle”. The energy gain empowers the particle to overcome the barrier earlier and thus increases  $\Gamma$ .

Martinis et al.<sup>25</sup> developed a theory to interpret the relative linewidth and strength of

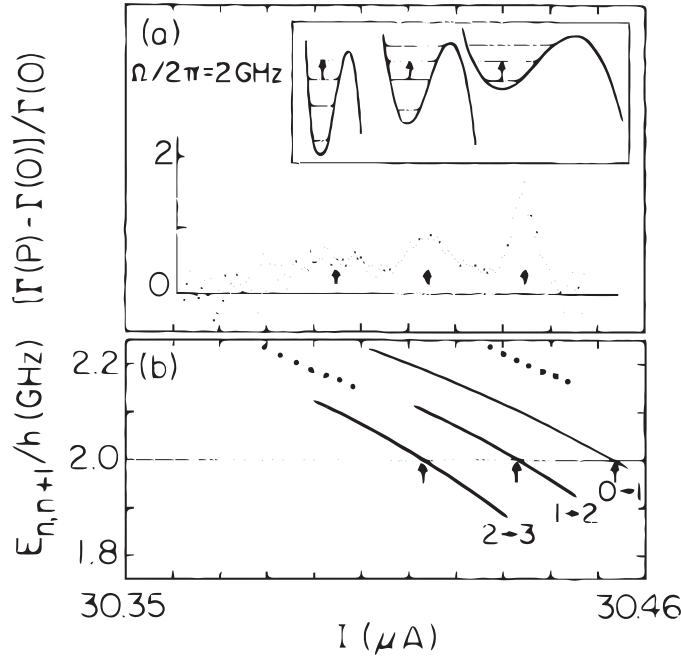


**Figure 2.6:** (a) Relative enhancement of  $\Gamma$  vs.  $I$  for a  $80 \times 10 \mu\text{m}^2$  junction in the presence of 2 GHz microwaves. The inset represents the transitions between energy levels for the current values corresponding to the peaks. (b) Calculated energy level spacing between states  $n$  and  $n+1$  ( $E_{n,n+1}$ ) vs.  $I$  for a specific junction. Dotted lines indicate uncertainties in the  $0 \rightarrow 1$  curve due to uncertainties in  $I_c$  and  $C$ . Arrows indicate values of bias current at which resonances are predicted. [25]

the resonances shown in fig. 2.6. They assumed a regime with only a few levels in the well. Equilibrium statistics leads to a modified escape rate (cf. equation (2.3))

$$\Gamma = \frac{\omega_a}{2\pi} \exp\left(-\frac{W - E_0}{k_B T}\right), \quad (2.23)$$

which takes the zero point energy of the ground state  $E_0$  into account. Martinis et al.<sup>25</sup> derived for the ratio of the relative populations of the energy levels  $f$  and  $f - 1$  with ( $r_f(P, \Omega)$ ) and without ( $r_f$ ) microwaves

$$r_f(P, \Omega) = r_f \frac{1 + \frac{\rho_{fi}(P, \Omega)}{r_f}}{1 + \rho_{fi}(P, \Omega)}. \quad (2.24)$$

Here,

$$\rho_{fi}(P, \Omega) = \frac{M_{i \rightarrow f}(P, \Omega)}{R_{f \rightarrow i}^T} \quad (2.25)$$

denotes the ratio of the transition rates from  $i$  to  $f$  induced by microwaves  $M_{i \rightarrow f}(P, \Omega)$  and the backreaction  $R_{f \rightarrow i}^T$  induced by resistance fluctuations.

Combining the above results (equations (2.24) and (2.25)) the enhancement of the escape rate can be described in the lowest order in  $r_f$  by

$$\gamma(P, \Omega) \equiv \frac{\Gamma(P, \Omega)}{\Gamma(0)} = 1 + \frac{\rho_{fi}(P, \Omega)}{r_f} . \quad (2.26)$$

Using atomic absorption spectra theory the frequency dependence of  $\rho_{fi}$  is expected to be Lorentzian with a center frequency  $\frac{E_{if}}{\hbar}$  and having a full width at half maximum of  $\frac{W_{if}}{\hbar} = \tau_i^{-1} + \tau_f^{-1}$ , where  $\tau_{i,f}$  are the lifetimes of the individual states. The final result for the relative population of states in the work of Martinis et al.<sup>25</sup> is equation (2.26) together with

$$\rho_{fi}(P, \Omega) = \frac{P}{2E_{fi}} \frac{\left( \frac{\tau_f^{-1} + \tau_i^{-1}}{2} \right)}{\left( \Omega - \frac{E_{fi}}{\hbar} \right)^2 + \left( \frac{\tau_f^{-1} + \tau_i^{-1}}{2} \right)^2} , \quad (2.27)$$

where  $\Omega/2\pi$  denotes the frequency of microwaves with power  $P$ . The experimental data of ref. [25] is exemplified in fig. 2.6, where the normalised increase of the escape rate dependence on the bias current is depicted in fig. 2.6 (a).

The experiments of Martinis et al. clearly showed for the first time the existence of quantised energy levels in the potential well by microwave spectroscopy. The positions of the energy levels in the well were shown to be in quantitative agreement with quantum mechanical calculations. Furthermore, the height and width of the resonance peaks were consistent with the simple model.

## Chapter 3

# QUANTUM COMPUTING

### 3.1 Quantum bits

Classical computers store information in units called bits (**binary digits**). These have the definite values of “0 or 1”, “up or down” or “true or false”. In real systems such a bit can be realised by the orientation of magnetic fields relative to an axis in one or the opposite direction, by a charged or uncharged capacitor, by simple DIP switches or -even more simple as in the early days- by the (non-)existence of holes in punchcards. Quantum information processing, in contrast, stores data in so called **quantum bits** (qubits). Physically, they can be realised by quantum two state systems. The values of the qubits are no longer definite, but can also be a superposition of the two states. The basis states of such a system can be denoted as  $|\uparrow\rangle$  and  $|\downarrow\rangle$ ,  $|0\rangle$  and  $|1\rangle$  or in matrix notation  $\begin{pmatrix} 1 \\ 0 \end{pmatrix}$  and  $\begin{pmatrix} 0 \\ 1 \end{pmatrix}$ . Therefore, the value of the qubit can be denoted as a wave function

$$|\Psi(t)\rangle = a(t)|\uparrow\rangle + b(t)|\downarrow\rangle \quad ,$$

with the probabilities of  $a(t)$  and  $b(t)$  for the qubit being in state  $|\uparrow\rangle$  and  $|\downarrow\rangle$ . Normalising this wave function

$$\langle\Psi(t)|\Psi(t)\rangle = a^2(t) + b^2(t) = 1$$

shows that the qubit state can be represented as a unit vector in the two dimensional Hilbert space  $\mathcal{H}_2$ . A graphical representation of this superposition (or wave function) is given by a vector on a Bloch sphere (fig. 3.1)

$$|\Psi\rangle = \cos\left(\frac{\Theta}{2}\right)e^{-i\frac{\phi}{2}}|0\rangle + \sin\left(\frac{\Theta}{2}\right)e^{+i\frac{\phi}{2}}|1\rangle \quad .$$

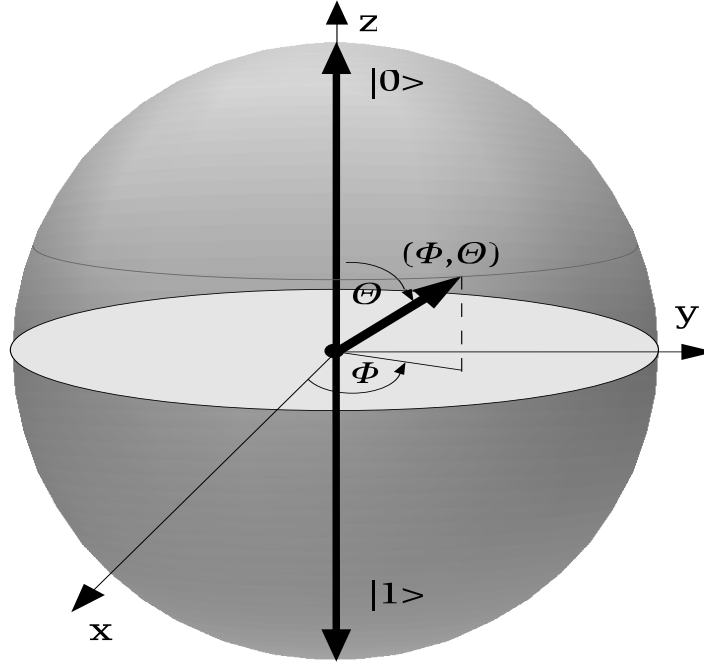


**Figure 3.1:** Representation of the qubit state  $(\Phi, \Theta)$  on the Bloch sphere.

The outstanding difference between quantum and classical systems is the possibility of entanglement, which can correlate classically pure states. For example, the wave function of a photon pair coming out of a nonlinear crystal cannot be described with the basis states

$$|10\rangle = |1\rangle \cdot |0\rangle \quad \text{and} \quad |01\rangle = |0\rangle \cdot |1\rangle, \quad (3.1)$$

where the state  $|0\rangle$  predicts no photon while  $|1\rangle$  predicts one for the 1<sup>st</sup> and the 2<sup>nd</sup> channel, respectively, but can only be described with wave functions including both states as for example the singlet state<sup>40</sup>

$$|\Psi_s\rangle = \frac{1}{\sqrt{2}}(|01\rangle - |10\rangle). \quad (3.2)$$

Thus while the information held in  $n$  classical bits scales as  $2 \times n$ , in qubits it scales as  $2^n$ . The enormous gain in computing power is due to the fact, that this gigantic amount of information held in qubits can be manipulated in one cycle by quantum gates (quantum parallelism).<sup>13</sup> On the other hand, quantum algorithms solving specific tasks are required to take advantage of this massive quantum parallelism. Up to now, only a small number of such algorithms is known: To name a few, P. Shor invented a quantum algorithm to factorise numbers.<sup>30</sup> The calculation time scales polynomially

with the length of the number whereas the best classical algorithm shows exponential scaling. The search algorithm invented by L. Grover provides a quadratic speed-up for searching databases.<sup>14</sup>

### 3.2 Superconducting qubits

Solid state based qubits can be produced by modern micro-/nanotechnology techniques (e.g. electron beam lithography) and therefore have the advantage of high scalability. On the other hand, due to these fabrication techniques their properties are not as well defined as for example in the case of individual ions in electromagnetic traps. On the other hand, the high flexibility of solid state based qubits allows to “install” enough knobs to compensate for this disadvantage.

In solid state based qubits usually many degrees of freedom are involved. In normal conducting devices the number of electrons in qubit circuits would be of the order of the Avogadro constant. One possibility to drastically reduce this huge amount of degrees of freedom is to use superconducting circuits. As explained in section 1.1 the electrons condensate to Cooper-pairs and one macroscopic wave function describes the superconducting state. Although quasiparticles exist which might induce decoherence, the superconducting energy gap strongly suppresses their creation at low enough temperatures. All in all we only have to deal with the coupling to the center of mass wave function in a good approximation.

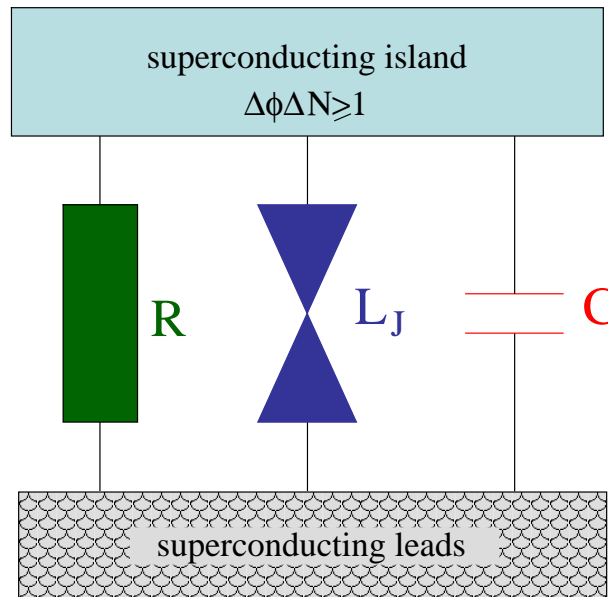


**Figure 3.2:** A superconducting island coupled to a superconducting lead (reservoir) via a Josephson junction characterised by an ideal Josephson element of Josephson inductance  $L_J$ , normal resistance  $R$  and a capacitance  $C$ . [13]

The principal types of Josephson junction based qubits will be illustrated by a superconducting island coupled to a superconducting electrode via a Josephson junction and a capacitor (see fig. 3.2). A commutation relation leads to the uncertainty relation  $\Delta\phi \Delta N \geq 1$  between the phase difference  $\phi$  across the Josephson junction and the number of Cooper-pairs on the island  $N$ . The relevant energy scales are the energy necessary to bring one additional Cooper-pair onto the island

$$E_C = \frac{q^2}{2C} \quad (3.3)$$

and the energy to change the phase difference by  $2\pi$

$$E_J = \frac{\phi_0 I_c}{2\pi} \quad (3.4)$$

Here  $q = 2e$  is the charge of a Cooper-pair and  $C$  is the capacitance of the capacitor. Obviously, if we can neglect thermal excitations ( $E_J, E_C \gg k_B T$ ) we can treat two limits:

- If  $E_C \gg E_J$ , the number of Cooper-pairs on the island is well defined since  $E_C$  is very large. The uncertainty relation then predicts a completely uncertain phase difference. In this case the Cooper-pair number on the island can be used as a qubit system (charge qubit).
- If  $E_C \ll E_J$ , the energy to change the number of Cooper-pairs on the island is negligible. Then, the number of Cooper-pairs is unclear and the phase difference is a well defined quantity. Thus, in this case the phase across the junction and therefore a current can be used as the qubit (persistent current qubit).

In the following I will concentrate on the persistent current qubit ( $E_C \ll E_J$ )<sup>1</sup>, which is in the main focus of the qubit research activities at the WMI. The most simple implementation is a rf (radio frequency) superconducting quantum interference device (SQUID) as shown in fig. 3.3.

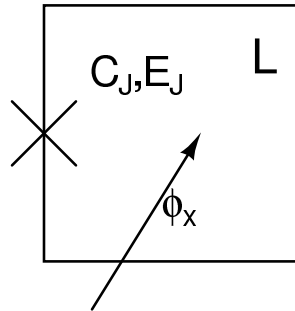


**Figure 3.3:** Sketch of a rf SQUID consisting of a superconducting loop of inductance  $L$  interrupted by a Josephson junction with coupling energy  $E_J$ , capacitance  $C_J$  and resistance  $R_J$ .

<sup>1</sup> The eigenstates are not actually flux eigenstates, so usually the term “persistent current qubit” is used, since the associated current is flowing clockwise or anticlockwise.

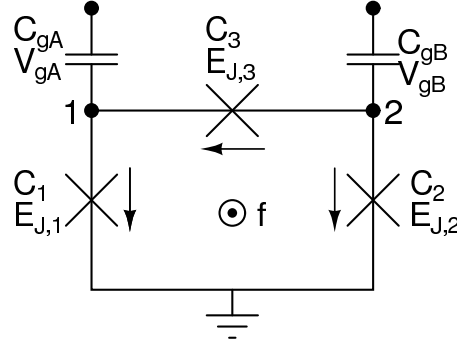


**Figure 3.4:** Persistent current qubit with three Josephson junctions.

The Hamiltonian of such a rf SQUID is given by

$$\mathcal{H}_C + \mathcal{H}_L + \mathcal{H}_J = \frac{q^2}{2C} + \frac{(\phi - \phi_x)^2}{2L} + E_J \left( 1 - \cos \left( \frac{2\pi\phi}{\phi_0} \right) \right) \quad , \quad (3.5)$$

where  $\phi_x$  is the externally applied flux,  $\phi$  is the total flux threading the loop,  $L$  is the loop inductance and the first term represents the kinetic energy (since  $E_C \ll E_J$  this term is smaller than the potential energy). The degenerate system used as qubit is obviously given by the second and third term around the degeneracy point  $\phi_x \rightarrow \phi_d = (n + \frac{1}{2})\phi_0$ . By looking at the potential energy (second and third term) it becomes obvious that  $L$  must be relatively large ( $\beta_L = \frac{2LI_c}{\phi_0} > 1$ ) to obtain a reasonable double well potential. This makes the structure sensitive to fluctuations of external magnetic fields. But there is the possibility to circumvent this problem using a modified structure with three Josephson junctions, which will be discussed in the next section. [13, 28, 31](#)

### 3.3 Persistent current qubit with three Josephson junctions

As described above the rf SQUID as simplest persistent current qubit structure suffers from a large inductance. This results in a high sensitivity to pick-up external stray fields and noise from control lines. Thus, T. P. Orlando et al. [28](#) suggested the structure shown in fig. 3.4. Here, two Josephson junctions with critical coupling energy  $E_{J,1} = E_{J,2} = E$  and capacitance  $C_1 = C_2 = C$  and one Josephson junction with coupling energy  $E_{J,3} = \alpha E_J$  and capacitance  $C_3 = \alpha C$  are inserted in a loop, which is capacitively connected by two capacitors  $C_{gA} = \gamma C$  and  $C_{gB} = \gamma C$  to ground. The dimensionless parameter  $\alpha$  is the knob to tune the qubit properties.

#### 3.3.1 The Hamiltonian

The arrows in figure 3.4 give the current directions for the following calculations,  $\varphi_n$  denotes the gauge invariant phase difference across the Josephson junction  $n$ . The

potential energy

$$U(\vec{\phi}) = E_J(2 + \alpha - \cos \phi_1 - \cos \phi_2 - \alpha \cos(2\pi f + \phi_1 - \phi_2)) \quad (3.6)$$

of the persistent current qubit (fig. 3.5) can be immediately derived using the potential energy of a Josephson junction  $U = E_J(1 - \cos \phi)$  and the fluxoid quantisation condition ( $\phi_2 - \phi_3 - \phi_1 = 2\pi f$ ), where  $f = \frac{\phi_x}{\phi_0}$  is the magnetic frustration. Thus, states which can be used as a qubit can be clearly identified in fig. 3.5. In this  $2\pi \times 2\pi$  pe-

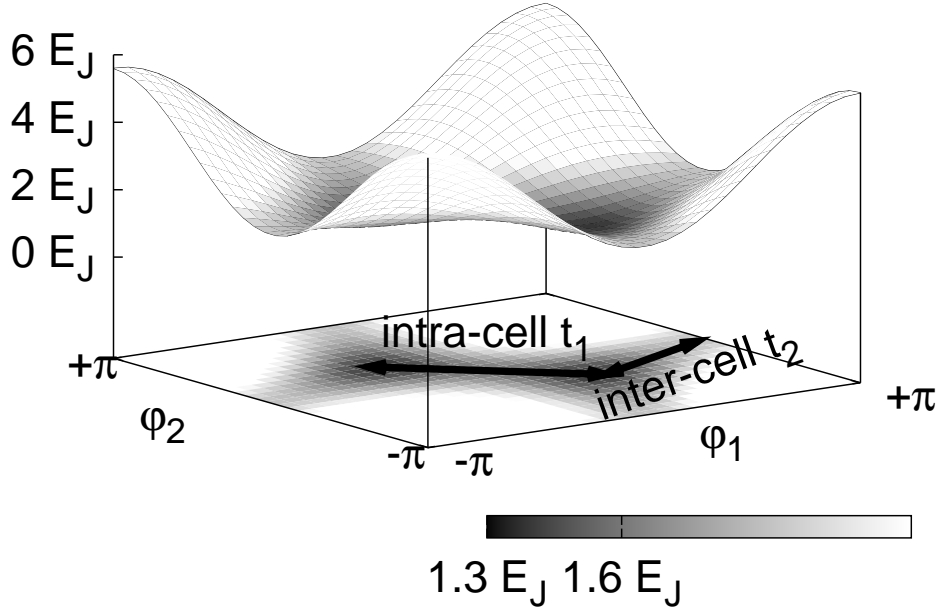


**Figure 3.5:** Potential of the Josephson persistent current qubit with  $\alpha = 0.8$ , frustration  $f = \frac{1}{2}$ . The arrows show intra-cell (probability  $t_1$ ) tunneling and inter-cell tunneling (probability  $t_2$ ).

riodic potential there is a probability  $t_1$  for tunneling between the minima shown in fig. 3.5, which is called intra-cell tunneling, and  $t_2$  for tunneling into a neighbouring unit cell, which is called inter-cell tunneling. The knob  $\alpha$  can be used to tune these two tunneling probabilities. Assuming that inter-cell tunneling is negligible,  $\alpha \approx 0.8$  is found to be the optimum.<sup>28</sup> Using the kinetic energy

$$T = \frac{1}{2} \sum_j C_j V_j^2 - Q_{gA} V_A - Q_{gB} V_B$$

the Hamiltonian

$$H = \frac{1}{2} \left( \vec{P} + \frac{\phi_0}{2\pi} \vec{Q}_g \right)^T \overleftrightarrow{M}^{-1} \left( \vec{P} + \frac{\phi_0}{2\pi} \vec{Q}_g \right) + U(\vec{\phi})$$

can be derived. Here, the canonical momentum  $\vec{P} = \begin{pmatrix} P_{\text{island 1}} \\ P_{\text{island 2}} \end{pmatrix}$  is directly proportional to the charges on the islands and  $\vec{Q}_g = C_g \vec{V}_g$  quantifies the charges on the islands. The mass matrix

$$\overleftrightarrow{M} = \left( \frac{\phi_0}{2\pi} \right)^2 \overleftrightarrow{C} \quad (3.7)$$

is anisotropic. To understand the potential's eigenfunctions the well known Bloch theory can be used.

### 3.3.2 The Bloch functions

The Josephson junction potential (3.6) is a  $2\pi \times 2\pi$  periodic function. From the theory of crystals we know that the solution of the Schrödinger equation for such a periodic potential is a complex exponential function times a periodic function. Therefore, we can split off  $e^{i\vec{k}\vec{\phi}}$  from the qubit solution  $\vec{\psi} = e^{i\vec{k}\vec{\phi}} \vec{\chi}(\vec{\phi})$  and get the Hamiltonian

$$H_t = \left( \frac{1}{2} \vec{P}^T \overleftrightarrow{M}^{-1} \vec{P} + U(\vec{\phi}) \right) \quad (3.8)$$

for this Bloch function.

### 3.3.3 Center of mass system

As utilised in the derivation of the coupled quantum mechanical harmonic oscillator it is advantageous to go to the center of mass system

$$\begin{pmatrix} \phi_1 \\ \phi_2 \end{pmatrix} \longrightarrow \begin{pmatrix} \phi_p \\ \phi_m \end{pmatrix} = \frac{1}{2} \begin{pmatrix} 1 & 1 \\ 1 & -1 \end{pmatrix} \begin{pmatrix} \phi_1 \\ \phi_2 \end{pmatrix} = \frac{1}{2} \begin{pmatrix} \phi_1 + \phi_2 \\ \phi_1 - \phi_2 \end{pmatrix}.$$

This leads to the transformed Hamiltonian

$$H_t = \frac{P_p^2}{2M_p} + \frac{P_m^2}{2M_m} + E_J (2 + \alpha - 2 \cos \phi_p \cos \phi_m - \alpha \cos (2\pi f + 2\phi_m)) \quad (3.9)$$

with associated canonical momenta  $P_p$  and  $P_m$  and the masses  $M_p = 2C(\phi_0/2\pi)^2(1 + \gamma)$  and  $M_m = 2C(\phi_0/2\pi)^2(1 + 2\alpha + \gamma)$ . Solving equation (3.9) for eigenfunctions results in two eigenstates  $u$  and  $v$ . Near the degeneracy point  $f_c = \frac{\phi_c}{\phi_0} = \frac{1}{2}$  the eigenstates associated with the current in the loop flowing clockwise and anticlockwise, respectively, are metastable.

### 3.3.4 Solution of the Schrödinger equation at $f = \frac{1}{2}$ — The tight binding model

In the weak coupling limit coupled potentials can be treated using the tight binding model. Here, the Schrödinger eigenfunctions

$$\Psi(\vec{\phi}) = c_u u(\vec{\phi}) + c_v v(\vec{\phi}) \quad (3.10)$$

are seen as a linear combination of the independent eigenfunctions  $u$  and  $v$  of the Hamiltonian  $H_t$ . The energy is offset by the average of the two lowest states. Then the Hamiltonian takes the form  $\begin{pmatrix} F & -t \\ -t & -F \end{pmatrix}$ , where  $\pm F$  represents the normalized eigenenergies of the states and  $t$  the coupling matrix element.  $\text{tr } H_t = \sum_n E_n$  and  $\det H_t = \prod_n E_n$  indicate that the eigenvalues are  $E_{1/2} = \pm \sqrt{F^2 + t^2}$ . The eigenvectors can be calculated to

$$\begin{pmatrix} \cos \frac{\Theta}{2} \\ \sin \frac{\Theta}{2} \end{pmatrix} \text{ and } \begin{pmatrix} -\sin \frac{\Theta}{2} \\ \cos \frac{\Theta}{2} \end{pmatrix} \quad (3.11)$$

where  $\Theta = -\arctan t/F$ , which obviously are the columns of the rotation matrix for rotations by an angle  $\Theta/2$ . So a principal axis transformation can be applied leading to the Hamiltonian matrix

$$\overleftrightarrow{H}_D = -\sqrt{F^2 + t^2} \begin{pmatrix} 1 & 0 \\ 0 & -1 \end{pmatrix} = -\sqrt{F^2 + t^2} \sigma_z, \quad ,$$

where  $\sigma$  denotes the Pauli matrices. This demonstrates that this system is worth being used for quantum information technology with a qubit represented in the eigenstates up  $|\uparrow\rangle = \begin{pmatrix} 1 \\ 0 \end{pmatrix}$  and down  $|\downarrow\rangle = \begin{pmatrix} 0 \\ 1 \end{pmatrix}$ .

### 3.3.5 The coupling matrix element $t$

As explained above it is necessary that the tunneling should only be possible between the two qubit states at  $(\varphi_p^*, \pm \varphi_m^*)$  and not into a neighbouring cell. So it is interesting to have a look at the associated tunneling matrix elements. In the following  $t_1$  is the tunneling parameter describing tunneling between the two minima representing the qubit states and  $t_2$  is responsible for inter-cell tunneling. To examine which tunneling term is dominant the WKB approximation can be used. Here, the tunneling probability is given by  $t_i \approx \frac{\hbar \omega_a}{2\pi} e^{\frac{1}{\hbar} S_i}$ .  $S_1$  and  $S_2$  can be approximated to<sup>28</sup>

$$S_1 \approx \hbar \sqrt{4\alpha(1+2\alpha+\gamma) \frac{E_J}{E_C}} \left( \sin \varphi_m^* - \frac{1}{2\alpha} \varphi_m^* \right) \quad \text{and}$$

$$S_2 = \hbar \sqrt{\frac{E_J}{E_C} \left( \frac{(1+\gamma) \left( 1 + \left( \frac{\pi-2\varphi_m^*}{\pi} \right)^2 \right)}{\alpha} + 2 \left( \frac{\pi-2\varphi_m^*}{\pi} \right)^2 \right)} \quad .$$

Inserting these expressions into the formula  $\frac{t_2}{t_1} \approx e^{-\frac{1}{\hbar}(S_2-S_1)}$  fig. 3.6 is obtained. The figure illustrates that flux qubits with  $E_J \gg E_C$  can be tuned in such a way that inter-cell tunneling becomes negligible.

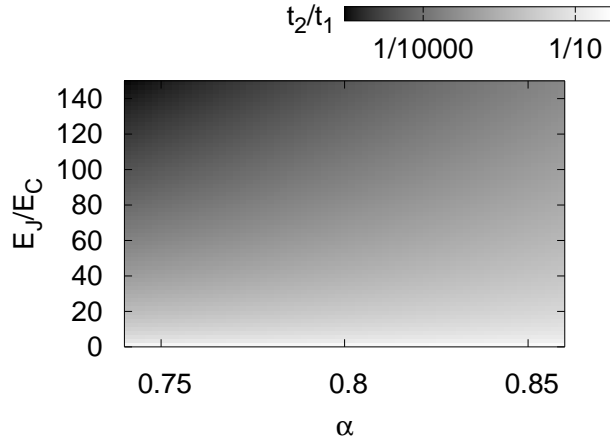


Figure 3.6:  $\frac{t_2}{t_1}$  plotted as a function of  $\alpha$  and  $\frac{E_J}{E_C}$ .

### 3.4 The DiVincenzo criterias and superconducting qubits

In the year 2000 D. DiVincenzo proposed seven essential requirements necessary for quantum computation systems (the last two of these only treat with quantum communication and will be skipped here)<sup>8</sup>. In the following I will discuss these criterias and to which extent superconducting qubits fulfill them<sup>31</sup>:

1. Scalable physical system with well characterized qubits  
Lithography is a convenient way to realise scalable qubits. The superconducting energy gap strongly suppresses problems with noise and decoherence. Varying device properties evolving in the fabrication process can be compensated for with tunable parameters.
2. Ability to initialize the qubit to a simple fiducial state  
If the level separation  $\Delta E$  is big compared to temperature ( $\Delta E \gg k_B T$ ) in thermal equilibrium the qubit is to a good approximation in the ground state.
3. Decoherence times much longer than gate operation time  
Important sources of decoherence in solid state based qubit systems are noise induced by the control lines and their vast degrees of freedom of thermally induced excitations. Decoherence in flux qubits may also be caused by quasiparticles, magnetic fluctuations, electromagnetic radiation and unwanted coupling to neighbouring structures. All in all the problem of decoherence seems to be solvable in lowest temperature setups.<sup>23, 35</sup>
4. “Universal” set of quantum gates  
Using electromagnetic coupling mechanisms usually opens a variety of possibilities to modify a Hamiltonian. Thus, already in the initial review of Orlando et

al.<sup>28</sup> simple gates like “one-qubit rotation” and “two-qubit controlled not” have been discussed.

5. Qubit specific measurement process

A variety of possibilities has been discussed for persistent current qubit readout. While using a simple SQUID magnetometer should be possible, more fancy setups are discussed presently<sup>38</sup>. Because of the significance of readout the readout scheme has to be carefully designed.

## Part III

# EXPERIMENTS



## Chapter 4

### EXPERIMENTAL SETUP

In this section I will describe the experimental setup including the low temperature equipment, the sample stage design including the junction mounting and the filter design.

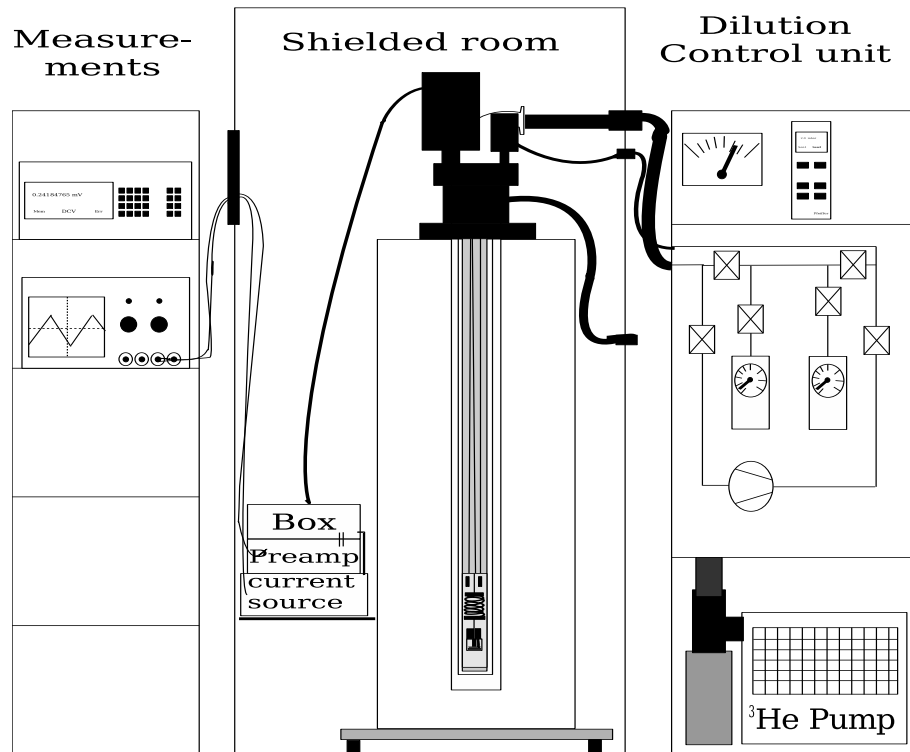


**Figure 4.1:** Schematic drawing of the experimental setup. In the middle the shielded room with the dilution unit in the cryostat, the battery powered current source and the preamplifier can be seen. On the left hand side the measurement devices are installed, while on the right hand side there are the pumping system, the gas handling system, and the temperature readout of the dilution unit.



**Figure 4.2:** Photograph of the experimental setup which is schematically shown in fig. 4.1.

### 4.1 Dilution refrigerator and low temperature setup

In the experiments a  $^3\text{He}$ - $^4\text{He}$  dilution refrigerator setup constructed at the WMI was used, which provides a minimal base temperature of about 20 mK (circulation rate  $25 - 30 \frac{\mu\text{mol}}{\text{s}}$ ). Due to the compact size this system has the advantage of short cooldown and warmup times, which allows (in the worst case of not working samples) almost a cycle per day. On the other hand, the limited experimental space at base temperature complicates the installation of microwave components for future experiments.

The setup (shown in figs. 4.1 and 4.2) consists of the dilution unit and a rack-mounted mobile control system. The latter one contains on the left side of the rack (front to the shielded room) the vacuum control equipment —mechanical and diffusion pump— and on the front side the helium gas handling system including the  $^3\text{He}$  circulation pump and a nitrogen cold trap to withhold water and other contaminants, which might get in the condensation line and tamp it. Two 15 liter tanks for helium mixture storage and emergency and pressure control sensors for the vacuum and the helium lines are also mounted there.

The dilution unit can be inserted into all cryogenic reservoirs with a two inch bore. In the experiments a glass fiber reinforced (“GFK”) cryostat was used, which was

mounted on a vibration damping base. Unfortunately, the damping of the  $^3\text{He}$  pumping line provided via a box containing sand was not sufficient to decouple the vibrations of the  $^3\text{He}$  circulation pump from the dilution unit.

Two concentric mumetal shields around the dewar and an additional cryoperm shield at 4.2 K have been installed to provide magnetic shielding. Care was taken not to use magnetic materials in the whole setup. The GFK cryostat has been placed in a shielded room which shields rf radiation up to 20 GHz.<sup>43</sup>

The vacuum connections between the dilution unit and the control unit were fed through the wall of the shielded room with commercially available and —if this was not possible— with self swivelled feed throughs; plastic centering rings have been used to completely galvanically disconnect the gas handling system from the shielded room, which was the main grounding point. For the  $^3\text{He}$  pumping line a 40 mm stainless steel pump hose was used to reduce the line impedance and thus increase the cooling efficiency.

#### 4.1.1 Temperature readout and sample heating

For temperature readout and heating a Picowatt AVS-47 resistance measurement bridge, which provides acceptable readout sensitivity with excitation voltages down to  $3\mu\text{V}$ , and the corresponding heater control unit TDS-530 have been used. To control the cooldown process at higher temperatures molybdenum sensors were selected, while for lowest temperature measurements home prepared Dale resistors are chosen (for a description of the preparation process see for example Ref. [34] and references therein). Due to the fact that most thermometers which are mounted in the dilution unit are only used for the warmup and cooldown process, the temperatures mentioned in this work only refer to one Dale sensor mounted at the sample stage.

The bridge is equipped with a preamplifier, which can be placed near the cryostat to reduce noise influencing the measurement process. Because of the high resistance of the temperature sensors of the order of a few ten kilo-ohms at base temperature, the strong temperature dependence of their resistance and since the system's base temperature is not in the ultralow temperature regime it was found neither necessary to use a four-point measurement nor to put the preamplifier in the shielded room. For the temperature readout the same LCR-filtered wiring scheme was chosen as for the actual measurements (see section 4.4.1).

For still, mixing chamber and sample stage heating the dilution insert is equipped with electrical resistors at these points. For connecting these heaters some of additional twelve lines are used, which are partially separated from the 48 lines used for temperature and junction measurements. These lines are also thermally anchored at 4 K, but less carefully filtered with sufficient attenuation only in the range between 100 kHz and 5 MHz. Hence, the sample stage heater was single stage RC filtered at 4 K with  $51\ \Omega$  in each of the lines and subsequent 750 pF between the lines resulting in a low-pass RC filter with cut-off frequency 2 MHz. While this should give sufficient filtering up to 1 GHz for the sample stage heater, there might be some noise heating of the mixing

chamber and still heater and furthermore, crosstalk to the measurement lines cannot be excluded.

The still heater is operated by a home made battery powered circuit. An empirically found constant current is used, which results in the lowest possible temperature at the sample stage.

For sample stage heating a low noise current source (Knick J-152) was used with constant currents up to 200  $\mu\text{A}$ .



**Figure 4.3:** Photograph of the dilution unit. The thermal anchoring at 4 K (1), the RC-filter PCB (2), the connectors (3) and the thermal anchoring (4) at Joule-Thompson temperature, the still with the subsequent heat exchanger (5) ending in the mixing chamber (6), and the shielded sample stage (7) can be identified.

## 4.2 Sample stage

### 4.2.1 Overview

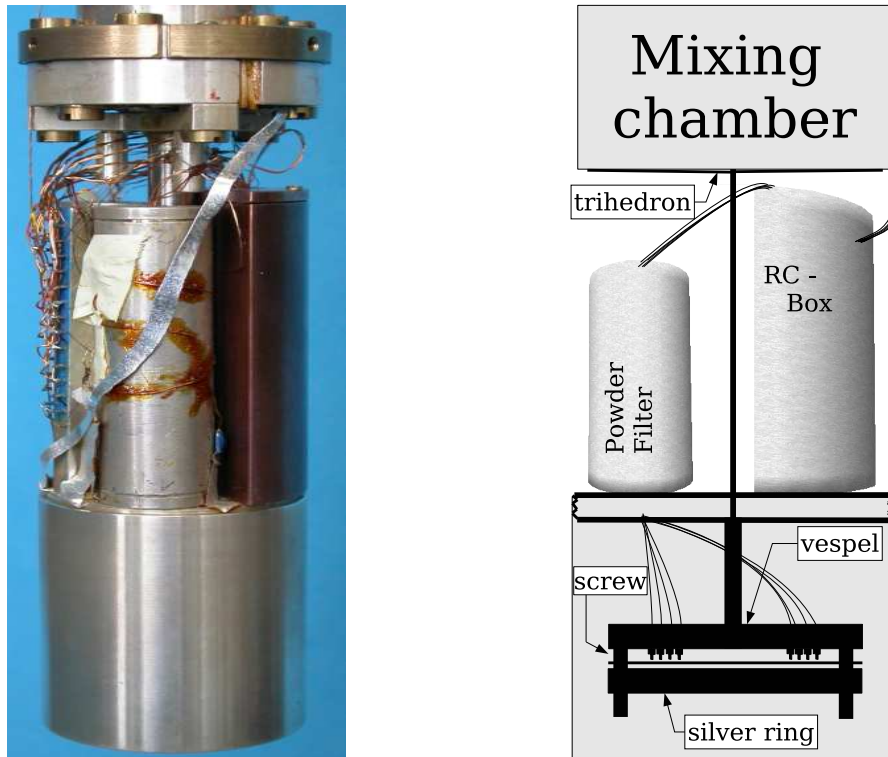


**Figure 4.4:** Photograph (left) and schematic drawing (right) of the sample stage below the mixing chamber. On the photograph the anchoring rod, where the wires coming out of the powder filter are soldered, and the thermal coupling are identifiable.

The sample stage (see fig. 4.4) is installed below the mixing chamber via a silver trihedron, in which a stainless steel shaft is screwed. Stainless steel is used because of its low thermal conductivity to thermally decouple the sample stage from the mixing chamber. A well defined thermal coupling between the sample stage and the mixing chamber can be established via an adjustable thermal conductor. The shaft ends in a round platform, which is made of sterling silver which provides good heat conductance and acceptable magnetic properties.

To seal the sample space hf tight a silver pot is screwed on a thread on the platforms outer rim. On the top of the platform two copper-in-powder filters and a RC-filter box (mK-box) are installed (see sections 4.4.2 and 4.4.3). The copper-in-powder filters are screwed with a hollow screw into the platform. Through the hole in the screws the wires enter the sample pot. The  $65\ \mu\text{m}$  copper wires coming from the powder filters are soldered at the top of gold-plated spring contacts clamped in a vespel disc (see fig. 4.6). With two screws a silver ring can be pressed against these spring contacts. In the space between the ring and the spring-contacts a silicon wafer can be clamped. On this



**Figure 4.6:** A wafer damaged by forces arising from different thermal expansion coefficients of the Si wafer and the silver ring (left) and the wafer mounting (right).

wafer the sample is mounted.

#### 4.2.2 Sputtering contacts and sample mounting

To establish electrical contacts to the sample gold contact pads were sputtered on a 1 inch silicon wafer through a laser-cut metal mask (see fig. 4.5). Care had to be taken that no gap between the wafer and the mask opened during the sputtering process to prevent short circuits between the gold lines. After sputtering the wafer had to be carefully examined.

To improve the adhesion of the gold layer, first a chrome layer was sputtered. The lines start on a 1.7 mm wide dot matching the pin configuration in the vespel and end near the middle of the wafer. There the sample with the junctions was glued and wire bonded to the gold lines with aluminum bond wires.

Since the aluminum bond wires become superconducting at low temperatures, the thermal conductivity and thus the cooling of the samples could be improved in future by using gold bonding wires (see section 4.3.1).

During cooldown the gold pins move a small distance on the gold pads. This becomes observable through small scratches which can be seen under the optical microscope. This might not be a problem for the electrical resistance between pin and wafer. A more severe problem are high mechanical forces exerted from the mounting on the wafer. This may lead to damage if there is not enough expansion space. Sufficient free space solves this problem.

In summary, this setup is more than sufficient to measure current-voltage characteristics which are important to evaluate the fabrication process. On the other hand, the insufficient heat anchoring makes measurements of escape rates a tricky thing, as will be seen in section 5.2.

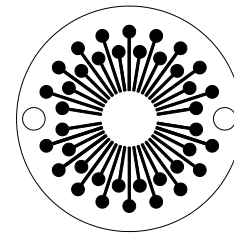


**Figure 4.5:** Sputtered structure with pads matching the vespel configuration

### 4.3 Wiring and filtering stages

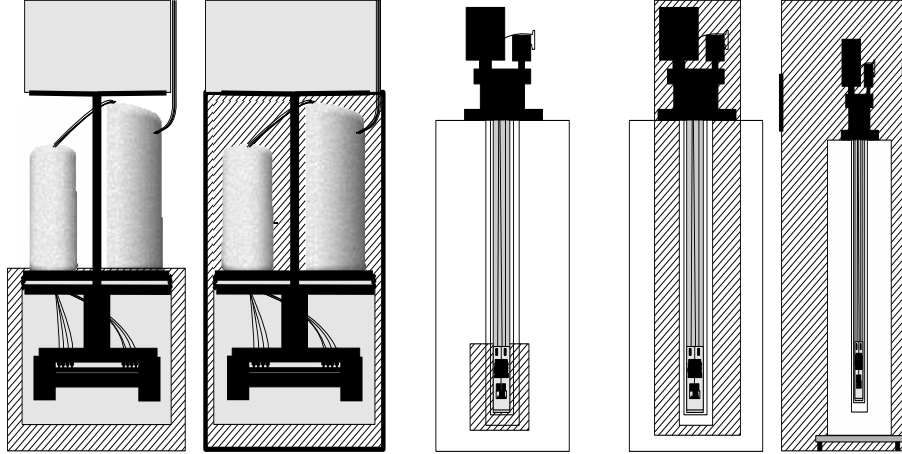


**Figure 4.7:** The hatched areas show the inner five shielding stages. From left to right the hermetically closed silver pot shielding the wires before the powder filters can be identified. The whole sample stage is shielded by the radiation shield. The vacuum chamber and the 4 K RC-filters attenuate high frequency signals. The last two pictures show the whole cryostat with mumetal shields and the shielded room.

In the description of the wiring I will start at the gold-plated spring contacts in the vespel disc and move upwards through the whole cryostat to the battery powered measurement devices and finally out of the shielded room.

On the gold spring contacts  $65\mu\text{m}$  diameter copper lines start going through the powder filters to the mK-box. Because the sample room is closed hermetically via a silver-pot and the powder filters it can be regarded as hf sealed and forms the *first shielding stage*. The lines coming out of the powder filters are soldered to pins in a anchoring rod in the mK-box (a solid metal rod, where isolated brass wires are glued in with “stycast 1266”). The RC-filter box was designed to house low-pass RC-filters. For the escape rate measurements on the niobium Josephson junction no RC-filter at this temperature stage was used because of the junctions huge critical current and the following heat dissipation. From the mK-Box a  $200\mu\text{m}$  copper wire connects to the central anchoring rod on top of the sample platform. There superconducting Nb wires in a CuNi matrix are soldered. These provide good thermal decoupling. The Nb-wires leave the *second shielding stage*, a brass radiation shield enclosing the whole sample stage, through small slits.

The superconducting wires end in the male part of gold-plated connectors. These connectors allow to disconnect the whole sample stage. The female parts —screwed to the flange at the exit of the Joule-Thompson heat exchanger ( $\approx 1.2\text{ K}$ )— are connected by  $100\mu\text{m}$  manganin wires to the PCB with the 4 K filters (see section 4.4.2). Although not well decoupled from the output, we might call this two stage RC-filters the start of the *third shielding stage*.

The cooling of the RC-filters is achieved via 200  $\mu\text{m}$  copper wires connecting the filter inputs to the central thermal anchoring rods made of copper, otherwise manufactured as above, at 4 K. These pins are the entrance of the measurement lines to the cold room in this inset.

To leave the cold environment 48 bronze wires are used. They end in an aluminum box (alubox) containing LCR-filters at room temperature (see 4.4.1). This can be regarded as the *fourth shielding stage*.

Two Amphenol 12-pin connectors mounted in the alubox establish electrical contacts to the outside.

For the measurements two connection cables ( $12 \times 0.14 \text{ mm}^2$  double-shielded cables) are used ending in a home-made brass box, which distributes the lines coming from the inset to BNC connectors. Here, the battery powered measurement devices—the preamplifier Stanford Research SR560 and the home made critical current detection electronics—are plugged in.

Through the *last shielding stage*, the shielded room, the BNC cables are fed through via commercially available BNC feed throughs.

#### 4.3.1 Thermal anchoring

Heat transport in solid state systems results from propagation of electrons and phonons. While the electronic conductivity in a metal remains acceptable unless the metal becomes superconducting at low temperatures, the Debye model predicts freezing out of phonons resulting in a thermal conductivity decreasing proportional to the third power of temperature. Thus in a millikelvin environment it is preferable to do thermal anchoring by metallic connections. Of course, electrical connections have to be isolated from ground, so the cooling of the device under test to base temperature has to be achieved somewhere via a phonon mechanism. It has been found that the heat generated in the device under test is best dissipated via the measuring lines, which can be anchored somewhere else.

The first bottleneck in removing heat from the junction are the aluminum bonding wires. Unfortunately, aluminum becomes superconducting, which is malicious for thermal conductivity. Bonding with gold wires was not successful because of sticking problems.

The next weak point are the gold pins; especially since there is still an unidentified resistance of the order of one ohm between the junction and the upper side of the pins which will cause some heating. Moreover, the thermal conductivity of the springs in the gold contacts is not known.

Although metallic wires are reasonable thermal conductors, the 65  $\mu\text{m}$  copper wires through the powder filters have a length of approximately 2 meters and thus represent a significant thermal resistance. Furthermore, even at low temperatures the copper lines have a finite electrical resistance and cause some heating.

Thus a silver flag with 200  $\mu\text{m}$  isolated copper wires wrapped around and encapsulated with blue stycast 2850 was mounted in the sample room. The ends of the wires were soldered to the spring contacts to provide thermal grounding. Due to minimal phononic heat conductivity of the stycast it is questionable whether this really improved the situation.

Furthermore, the lines are thermally anchored as good as possible at the sample stage, at the mixing chamber, at the heat exchanger and at 4K.

## 4.4 Filters and current dividers

To prevent the Josephson junction from noise or rf radiation induced switching to the voltage state, the sample space has to be shielded against this external influences. Therefore, four filter stages are built into the cryostat:

1. a LCR-filter stage at room temperature (section 4.4.1)
2. a double RC-filter stage after the 4 K thermal anchoring (section 4.4.2)
3. a double RC-filter stage in the mK-RC-box, which is not used in the escape rate experiments described in chapter 5 because of the high critical current of the Josephson junction resulting in a significant heating of the RC-filters
4. a copper-in-powder filter stage (section 4.4.3)

The RC- and RCL-filters are realized on printed circuit boards. SMD components are used to save space and to minimise parasitic effects. The capacitors are realised with two or three Kemet C0805 capacitors in parallel to reduce equivalent series inductance (ESL). Allowing for more space between the capacitors in parallel would certainly increase the efficiency in future setups.<sup>44</sup>

In contrast to usual filter designs I have used the input impedance in both input lines. The reason for this is to also filter the ground lines, which might be a potential access for rf noise. Thus the lines are floating in the cryostat.

### 4.4.1 The warm LCR filters

The first filter is designed to operate at room temperature. Its purpose is to filter out as much high frequency signals in the lines going down into the cryostat as possible. Another aspect is that the filter itself must definitely not insert too much noise, which occurs if too high resistance values are used. For the desired frequency using a second order RC circuit would require a resistance of at least 20 k $\Omega$  resulting in an intolerable amount of Johnson-Nyquist noise introduced by this circuit.

Therefore, damped LCR circuits were used, though if not properly designed these filters may introduce resonances. The cutoff frequency should be as low as possible. Due to incompatibility of the home made current source with large capacitors and the

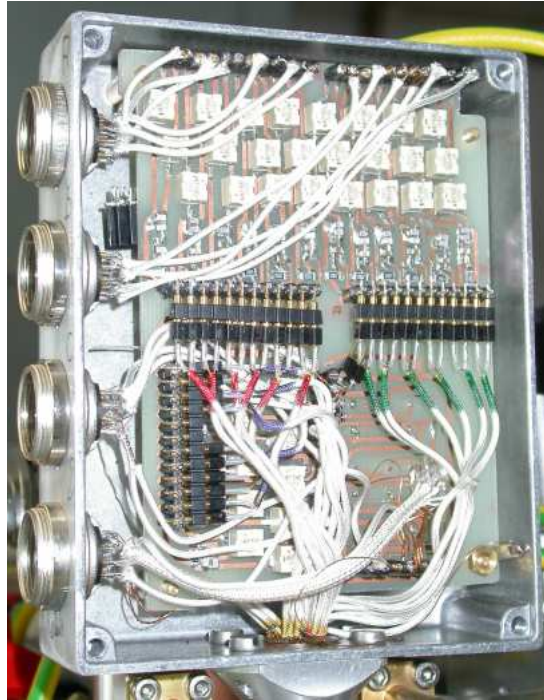


**Figure 4.8:** Photograph of the LCR-filters at room temperature. The filters at the bottom can be grounded via monostable relays. A part of the upper filters is used for the temperature sensors.

high parasitic series resistance of large capacitors,  $C_b = 2 \times 100 \text{ pF} = 200 \text{ pF}$  were chosen. The limitations imposed on the inductances are given on the one hand by the resistance of the coils which introduces Johnson-Nyquist noise and, on the other hand, by the capacitive coupling in the coils due to a large number of windings. A  $L = 4.7 \text{ mH}$  inductor was found as a compromise. Therefore, a filter with cut-off frequency of  $f_{\text{cutoff}} = \frac{1}{2\pi\sqrt{LC}} \approx 100 \text{ kHz}$  was designed.

This circuit has to be damped correctly. The following possibilities require only one resistor:<sup>20</sup>

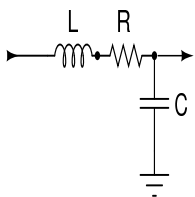


**Figure 4.9:** R in series  
 $R_{\text{crit}} = 2\sqrt{\frac{L}{C}}$

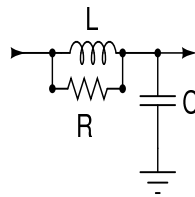


**Figure 4.10:** L, R in parallel  
 $R_{\text{crit}} = \frac{1}{2}\sqrt{\frac{L}{C}}$

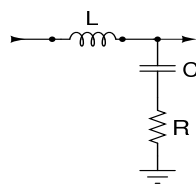


**Figure 4.11:** Damped by-pass  
 $R_{\text{crit}} = 2\sqrt{\frac{L}{C}}$

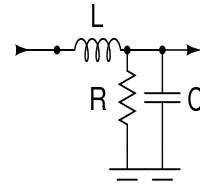


**Figure 4.12:** Resistor to ground  
 $R_{\text{crit}} = \frac{1}{2}\sqrt{\frac{L}{C}}$

The critical resistance  $R_{\text{crit}}$  thereby defines the resistance needed to critically damp the LCR circuit.

The circuit in fig. 4.9 obviously gives the best attenuation at high frequencies, but uses a resistor in series introducing Johnson-Nyquist noise. Putting inductance and resistor in parallel (fig. 4.10), which is the circuit initially used in the cryostat and is still used to filter the heater lines, gives unacceptable damping at high frequencies (almost no damping above 5 MHz with the above values). Damping the bypass as in fig. 4.11 obviously decreases the filter effectiveness. The last alternative (fig. 4.12) suffers from high power consumption.

Thus all resistor solutions are not satisfactory. That is why a solution published by K. Kundert<sup>20</sup> was used. A combination of the circuits in fig. 4.11 and 4.12 was built including the filtered ground already mentioned:

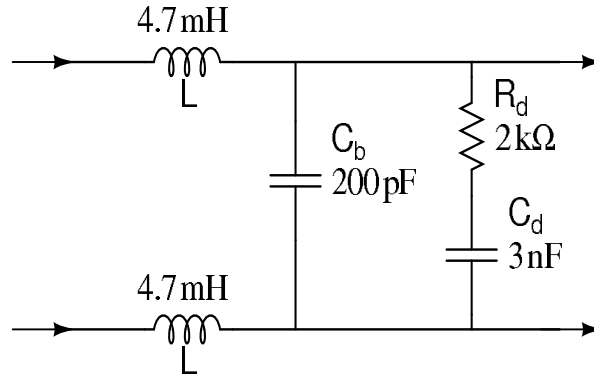


**Figure 4.13:** Schematic of room temperature LCR filters

A larger capacitor  $C_d$  in series with a resistor  $R_d$  damps the network while the bypassing is realized via a parallel bypass capacitor  $C_b$ . To get an idea of the size of the required resistor one can have a look at the critical dampings of the networks  $L, R_d$  and  $C_d$  and  $L, R_d$  and  $C_b$ . As a result one gets

$$R_d \gtrsim R_{crit,(L,R_d,C_d)} = 2\sqrt{\frac{L}{C_d}} \approx 3.5 \text{ k}\Omega \quad \text{and} \quad (4.1)$$

$$R_d \lesssim R_{crit,(L,R_d,C_b)} = \frac{1}{2}\sqrt{\frac{L}{C_b}} \approx 3.4 \text{ k}\Omega \quad . \quad (4.2)$$

The 2 k $\Omega$  resistances used turned out to be a compromise. The parasitic resistances of the inductances of approximately 40  $\Omega$  provide some damping, too.

The cut-off frequency of this filter is about 100 kHz and as long as parasitic effects can be neglected the increase of the attenuation should be 40  $\frac{\text{db}}{\text{decade}}$ .

## 4.4.2 RC filters and current dividers

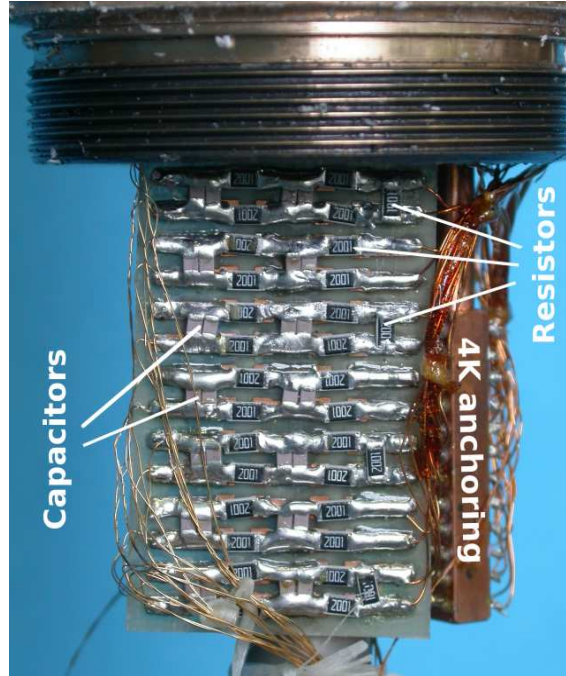


**Figure 4.14:** Photograph of the RC filters at 4 K.

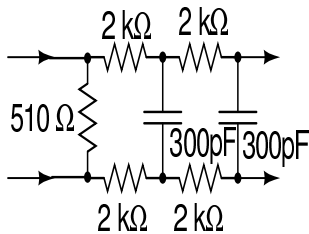


**Figure 4.15:** Schematic of a RC filter containing current dividers

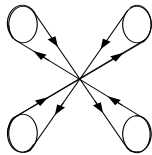
At 4 K and in a box at the sample stage RC-filters including current dividers are installed. At 4 K, they are realised on a printed circuit board (PCB) holding 8 double RC filter stages on each side of the PCB. The current dividers are realised by a resistor between a pair of lines coming into the filter. For the measurements presented in chapter 5 a circuit as shown in the schematic 4.15 has been used. Under the assumption that the junction resistance is negligible compared to  $4 \times 2 \text{ k}\Omega$  of the filters, the  $510 \Omega$  resistor between a pair of lines results in a current division of  $510 \Omega : 8 \text{ k}\Omega = 1 : 15.7$ . For thermal anchoring the electrical connections have been used.

The PCB at millikelvin temperature is only etched on one side, while the back side is covered by a copper layer for thermal grounding. In the measurements presented in chapter 5 no filter was used at this stage because of excessive heat generation due to the large critical currents of the niobium junction.

### 4.4.3 Copper-in-powder filters

Signals with frequencies in the GHz-range cannot be attenuated with ordinary RC or LC filters made from discrete elements due to parasitic effects (one exception for this might be the miniature electrical filters operating at cryogenic temperatures reported by Vion et al.<sup>39</sup>). Therefore, in 1987 Martinis et al.<sup>25</sup> developed a filter consisting of a “Manganin wire inside a copper tube filled with copper powder with a grain size of about 30  $\mu\text{m}$ ”. The naturally grown oxide layer insulates the grains against each other creating an enormous surface. So skin-effect-damping occurs. In ref. [25] an attenuation of more than 50 db in the range from 0.5 to 12 GHz is obtained with 0.1 m wire. Nowadays these filters are state-of-the-art for sensitive low temperature measurements, but today stainless steel often is used instead of copper. Although at room temperature the attenuation of copper- and stainless-steel filled filters are nearly the same, the copper filter efficiency degrades approximately by 50 % due to the decrease of the resistance of copper at helium temperature resulting in lower dissipation, while the resistivity of stainless steel stays nearly constant producing nearly the same attenuation at low temperatures.<sup>11</sup>

In the experiment two powder filters –one holding 4 and the other holding 8 twisted copper wire pairs with a diameter of 65  $\mu\text{m}$ – have been produced in this way:



Approximately 1.5 meter twisted wires were wound around a wiring tool (four metal rods in a holder) into a double eight shaped form as shown in the picture on the left hand side, where each “eight” holds half of the wires. The wiring tool together with the wires was inserted into a silver tube with a diameter of 1.2 cm. Next the wiring tool was carefully removed leaving the wires in the double-eight shape in the housing and stainless steel powder<sup>1</sup> was filled in. The powder in the tube was concentrated in an ultrasonic bath to get rid of non-damping empty space. Finally, the top and the bottom of the filter were sealed vacuum tight with epoxy stycast 1250. As reported in ref. [11] due to the low viscosity it penetrates into the powder. This on the one hand replaces some powder resulting in lower damping, but on the other hand should provide a better thermal coupling.<sup>11</sup> The penetration can be controlled by prehardening the stycast.

It is found that the double-eight shape of the wires is extremely stable — even after several cool down cycles opening the filters and removing the powder makes the double-eight form reappear.

To test the quality of the filters a test tube with two SMA connectors and the above described wire-in-powder insert was produced. A measurement of the attenuation recorded with a HP 8722 D vector network analyzer is shown in fig. 4.16. The experiment is calibrated against a short wire put into the tube without powder. The frequency dependence of the transmission parameter  $S_{12}$  is shown as blue line. At frequencies of

<sup>1</sup> Stainless Steel flake, –325 mesh, 0.83 micron thick, Type 316-L; Formula: Fe:Cr:Ni:Mo 67.5:17:13:2.5 wt%

some GHz the attenuation reaches the noise floor of the instrument (green line). Using this setup (HP 8722 D) it cannot be clarified if the performance of the filters is comparable to the data in ref. [3]. The experimental data discussed in chapter 5 suggests that the attenuation is sufficient to observe MQT.

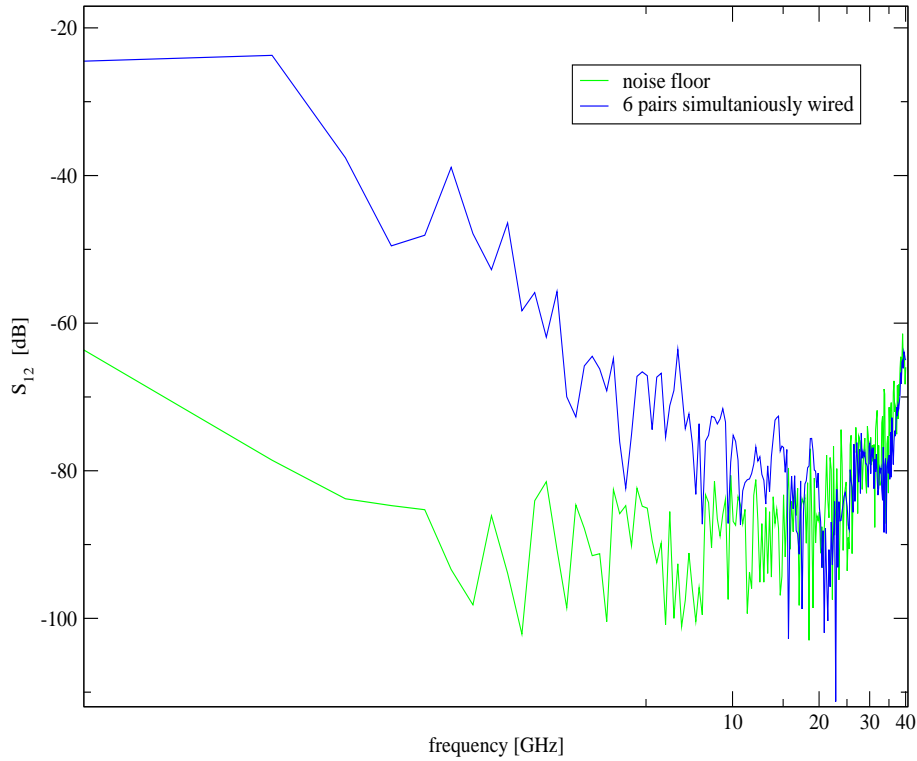


**Figure 4.16:** Transmission parameter  $S_{12}$  of a twisted six wire test powder filter vs. frequency (blue line). The noise floor of the spectrum analyzer is given by the green line.



## Chapter 5

### EXPERIMENTS AND RESULTS

The development of the experimental setup can be divided in two major steps. In the first step, the basic setup was installed and tested while in the second cycle the various filtering stages at different temperatures, the thermal coupling of the sample stage and the wiring properties were characterised and optimised.

In the basic development phase current-voltage ( $I$ - $V$ -) characteristics of home made Al/Al<sub>2</sub>O<sub>3</sub>/Al Josephson junctions were taken to assure that the wiring and the wafer mounting were working (see section 5.1). Furthermore, these measurements were necessary to support the junction technology.

During the advanced development phase, the low-pass filtering was characterised by investigating the escape rates of Nb/Al<sub>2</sub>O<sub>3</sub>/Nb Josephson junctions. Only after installing additional filter stages, reasonable data for the escape rates could be obtained. Furthermore, the escape rate measurements have been hindered by thermal coupling issues.

## 5.1 $I$ - $V$ -Characteristics

During the development phase  $I$ - $V$  characteristics of home made Al/Al<sub>2</sub>O<sub>3</sub>/Al Josephson junctions<sup>17</sup> like the one shown in fig. 5.1 have been acquired to get a feeling for the connection reliability and to support the junction manufacturing process. An important parameter in the process of tuning the barrier thickness was the critical supercurrent density.

For these early measurements, the filtering described in section 4.4 was not developed. LCR-filters, which were initially designed to reduce noise heating, provided only negligible filtering above 5 MHz. An unexpected feature often observed in the  $I$ - $V$ -characteristics is marked in fig. 5.1 by arrows. Comparing these features with fig. A.3 in ref. [45] suggests that it might be related to the insufficient filtering.

An important parameter to evaluate the junction quality and thus the manufacturing process is the  $I_c R_n$  product. For the junction shown in fig. 5.1  $I_c R_n \approx 155 \mu\text{V}$  is obtained. From theory a value of  $280 \mu\text{V}$  is expected. Thus the experiment quite well agrees with the theory.

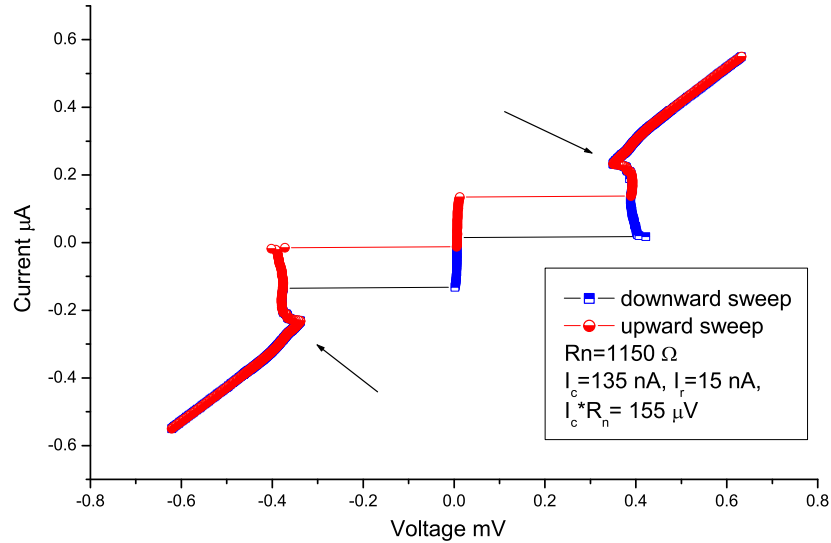


**Figure 5.1:**  $I$ - $V$ -characteristics of an Al/Al<sub>2</sub>O<sub>3</sub>/Al Josephson junction taken at  $T \gtrsim 28$  mK with the first inefficient LCR-filters at room temperature and without RC-filters at low temperature.

Figure 5.2 shows the current-voltage-characteristics of the Nb/Al<sub>2</sub>O<sub>3</sub>/Nb Josephson junction, which has also been investigated in the escape rate measurements (see section 5.2). Due to the large value of the critical current and the consecutive excessive heating, when the junction switches to the voltage state, only a small part of the  $I$ - $V$ -characteristics was traced out (see fig. 5.3). Heating is probably also responsible for the unexpected curvature of the current-voltage characteristics for negative currents exceeding the critical current.

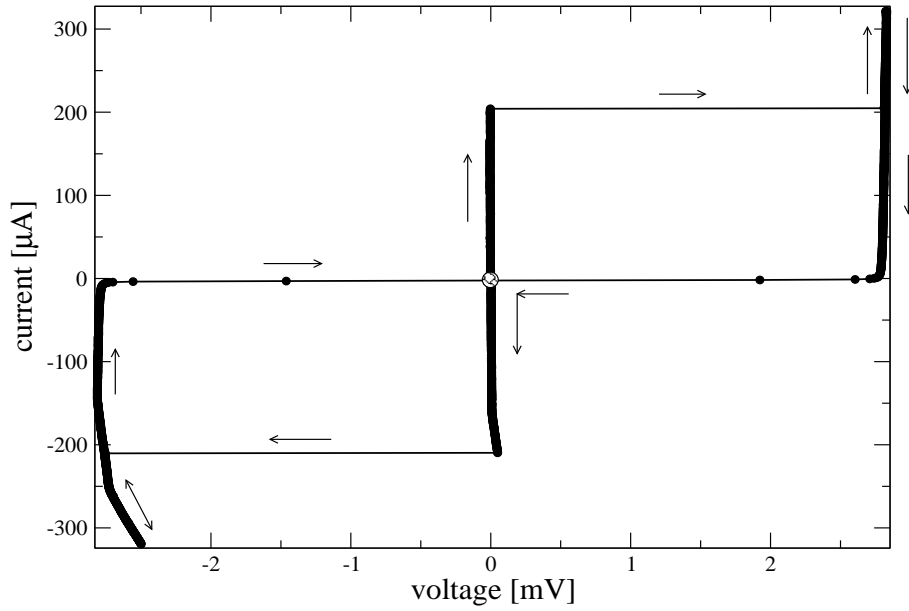


**Figure 5.2:** *I-V*-characteristics of the Nb/Al<sub>2</sub>O<sub>3</sub>/Nb Josephson junction used for the escape rate measurements at  $T \gtrsim 28$  mK (measured with the filtering described in section 4.4). The arrows indicate the direction of current sweep.

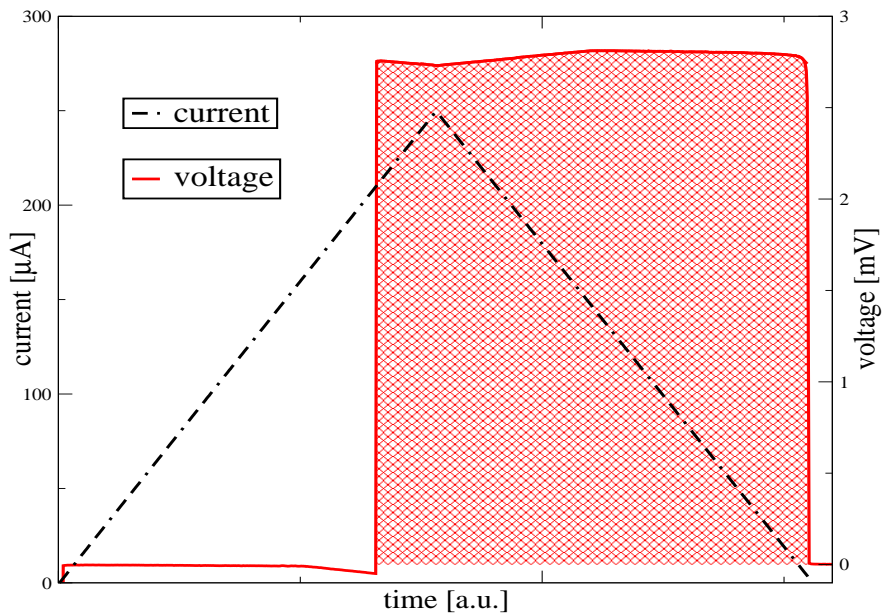


**Figure 5.3:** Voltage and current across the Nb/Al<sub>2</sub>O<sub>3</sub>/Nb Josephson junction vs. time. There is no heating during ramping up the current, while in the hatched region (voltage state) energy is dissipated.

## 5.2 Escape rate measurements

In escape rate measurements the probability of a Josephson junction switching from the zero voltage state into the finite voltage state depending on the bias current is measured. There are (at least) two possible experimental realisations: Firstly, one ramps a current from zero until the junction switches into the finite voltage state (“ramping experiments”), secondly, one determines the lifetimes of the zero voltage state at a specific current. The advantage of the first approach is a quasi-continuous histogram, which is obtained, while in the latter approach one has to calibrate the current for each measurement. Thus the experiment described in this work used the ramping technique.

The experiments have been performed on Nb/Al<sub>2</sub>O<sub>3</sub>/Nb Josephson junctions, which have been previously extensively characterised by escape rate measurements by T. Bauch at the Chalmers University of Technology, Sweden.

The experimental challenge was to acquire a histogram of the currents, where the junction switches during a well defined current ramp (see section 5.2.1). From these data the escape rate  $\Gamma$  as a function of current has been calculated leading to characteristic escape temperatures as described in section 5.2.2.

### 5.2.1 Measurement setup

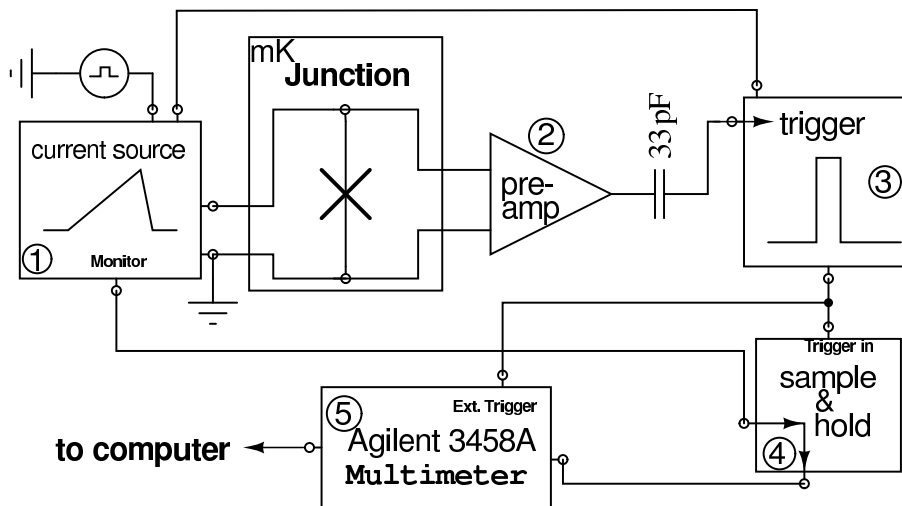


Figure 5.4: Schematics of a current ramping experiment.

The junctions were connected in a four-probe setup using two pairs of twisted wires for current feed and voltage probe. The current ramp was provided by a home made analog current source (marked 1 in fig. 5.4), which feeds a low-noise sawtooth current signal to the junction. The lower limit of the ramp was set a bit below zero to assure that the junction switches back from the voltage state to the superconducting state, the

upper limit was dynamically given by the switching of the junction.

The voltage across the junction was amplified using a Stanford Research SR560 low-noise voltage preamplifier (2) by a factor of 500, typically. The amplified signal was used to detect the switching of the junction in a trigger unit (3). The trigger signal was given to the current source to change the ramping direction, initiates a cycle feeding the current magnitude into the “Sample & Hold” module (4) and triggered the multimeter Agilent 3458A to read out this value with a typical integration time of about 200 ms. The values have been stored in the multimeter’s internal memory and after a certain number of data they were transferred to a computer and stored in a ASCII file for later evaluation.

Unfortunately, for the best measurements up to now no twisted voltage probe wires could be used, therefore, mutual inductance prevented ramp times less than 10 ms. Another severe problem was thermal heating in the junction and probably in the vicinity of the vespel disc. By varying the duty cycle it could be shown, that for duty cycles  $>1.7$  s heating is no longer a problem. On the other hand, due to this long duty cycles, the histograms were limited to 2000 samples.

Figure 5.5 shows an example of such an experiment taken at 28 mK. In fig. 5.6 a histogram of the decay probability depending on the bias current is shown. It turned out that for the data evaluation it is necessary to limit the fit to a region in the histogram with reasonable amount of data. Typically, the histogram was evaluated with 100 channels, as described in the next section.

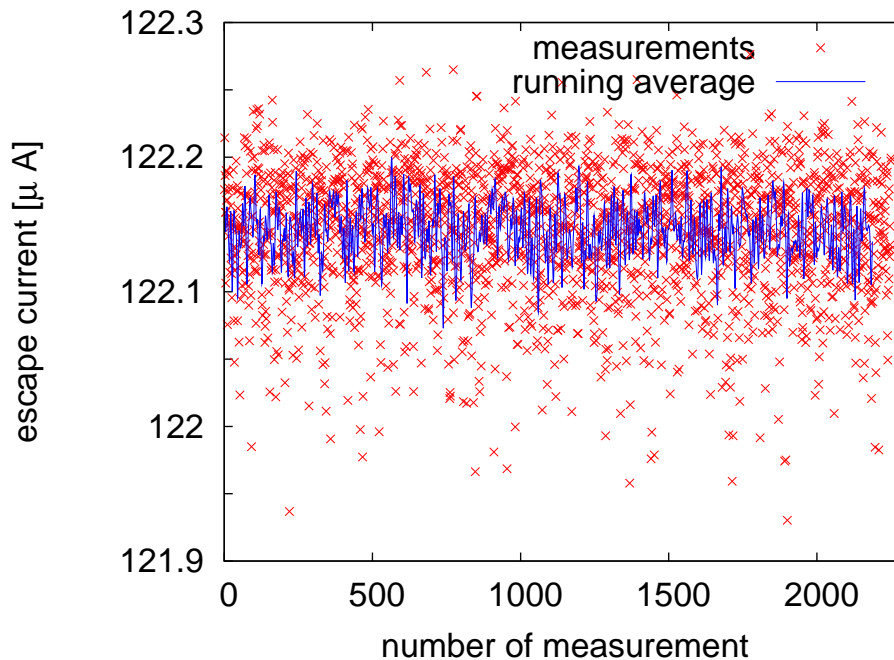


**Figure 5.5:** Measured values for the switching current  $I_c$  at 28 mK (symbols) and the 15 point running average of the data (solid line) to identify changes of  $I_{c0}$  indicating temperature instability.

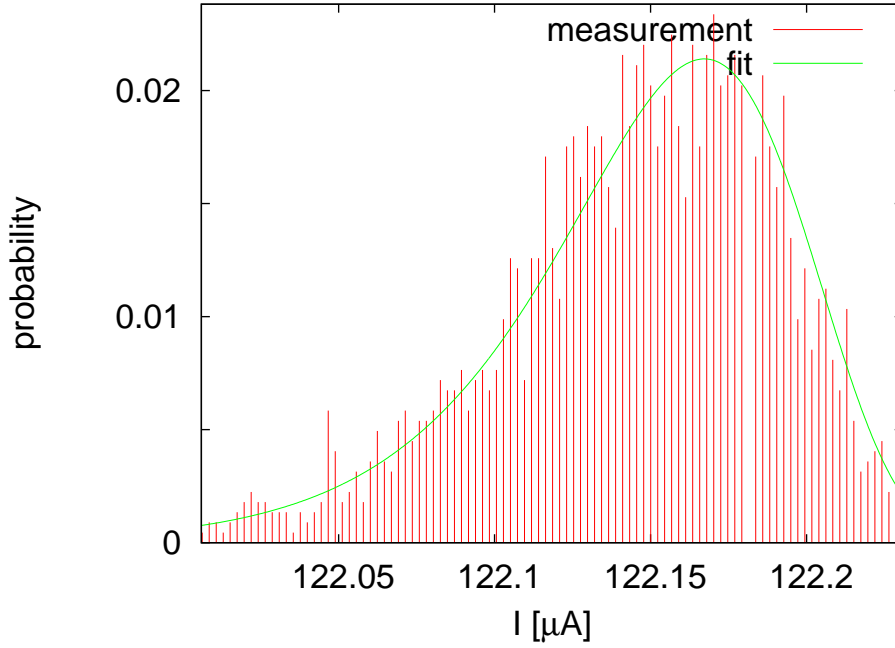


**Figure 5.6:** Histogram of the switching current between the limits 122  $\mu\text{A}$  and 122.23  $\mu\text{A}$  at 28 mK evaluated from the data shown in fig. 5.5.

### 5.2.2 Data evaluation

The data evaluation is based on a method originally developed by T. Fulton and L. Dunkleberger.<sup>12</sup> Here, the histogram of the critical currents as shown in fig. 5.6 is used. From this histogram the escape rate depending on the bias current can be calculated. The probability  $p(I_b)$  for a junction in the zero voltage state to switch to the running state at bias current  $I_b$  (evaluated in the channel between  $I_b$  and  $I_b + \Delta I$ ) is given by<sup>12</sup>

$$p(I_b) = \int_t^{t+\Delta t} \Gamma(t) e^{-\Gamma(t) \frac{dt}{dI_b(t)} (I_b(t') - I_b(t))} dt' ,$$

where the values of  $t$  correspond to the appropriate current values,  $\frac{dI_b}{dt}$  denotes the ramping velocity, and  $\Gamma$  stands for the escape rate, which is the parameter to be calculated. The normalised probability of escape in a specific channel  $N(I_b)$  can be evaluated to

$$p(I_b) \equiv \frac{\sum_{n=\hat{n}(I_b)}^{\hat{n}(I_{max})} N(I_b(n)) - \sum_{n=\hat{n}(I_b)+1}^{\hat{n}(I_{max})} N(I_b(n))}{\sum_{n=\hat{n}(I_b)}^{\hat{n}(I_{max})} N(I_b(n))} ,$$

where  $\hat{n}(I_b)$  denotes the number of the channel associated with bias current  $I_b$ . Simple algebra gives the expression

$$\Gamma(I_b) = (\Delta I)^{-1} \frac{dI_b}{dt} \ln \left( \frac{\sum_{n=\hat{n}(I_b)}^{\hat{n}(I_{max})} N(I_b(n))}{\sum_{n=\hat{n}(I_b)+1}^{\hat{n}(I_{max})} N(I_b(n))} \right) \quad (5.1)$$

for the escape rate  $\Gamma$ . Figure 5.7 shows  $\Gamma(I_b)$  for the data in figs. 5.5 and 5.6.

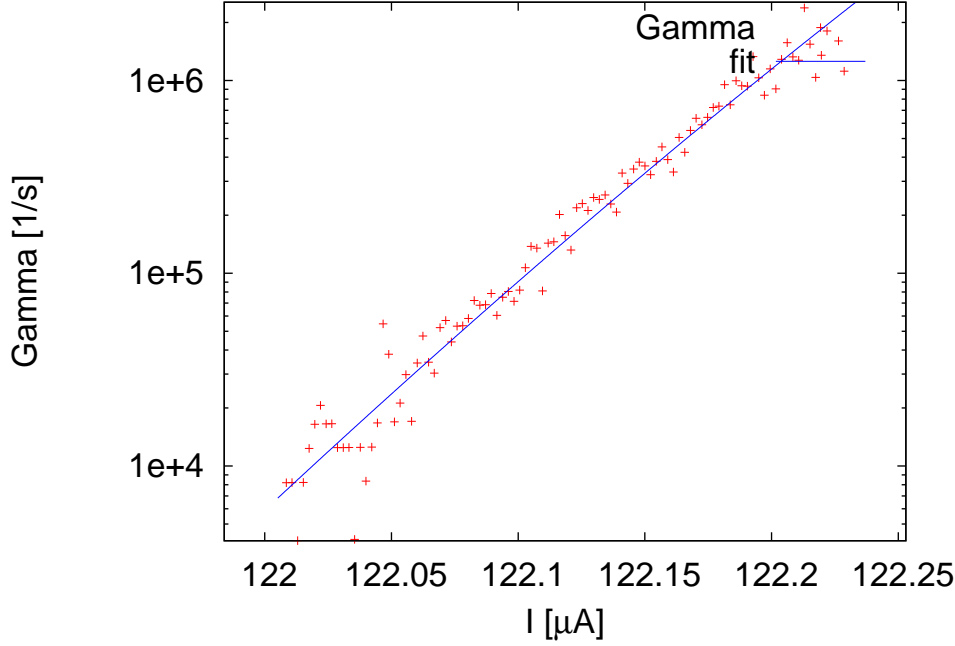


**Figure 5.7:** The calculated values of  $\Gamma$  at 28mK depending on the bias current (for the data shown in fig. 5.5).

Using the definitions of section 2.4 (equations (2.8) and (2.16)) and plotting

$$\left( \ln \frac{\omega_p}{2\pi\Gamma(I_b)} \right)^{2/3} \quad (5.2)$$

versus the bias current, a straight line with slope  $\left( \frac{I_c \phi_0 2\sqrt{2}}{3\pi k_B T_{esc}} \right)^{2/3}$  can be fitted to the data.<sup>7</sup>

A plot of  $\left( \ln \frac{\omega_p}{2\pi\Gamma(I)} \right)^{2/3}$  of the data shown in fig. 5.5 vs.  $I_b$  together with a linear fit is shown in fig. 5.8. A limiting factor is the uncertain attempt frequency  $\omega_a$ , which was estimated with the junction capacitance of  $C = 1$  pF via equations (1.9) and (2.9). Later the plasma frequency can be determined spectroscopically.

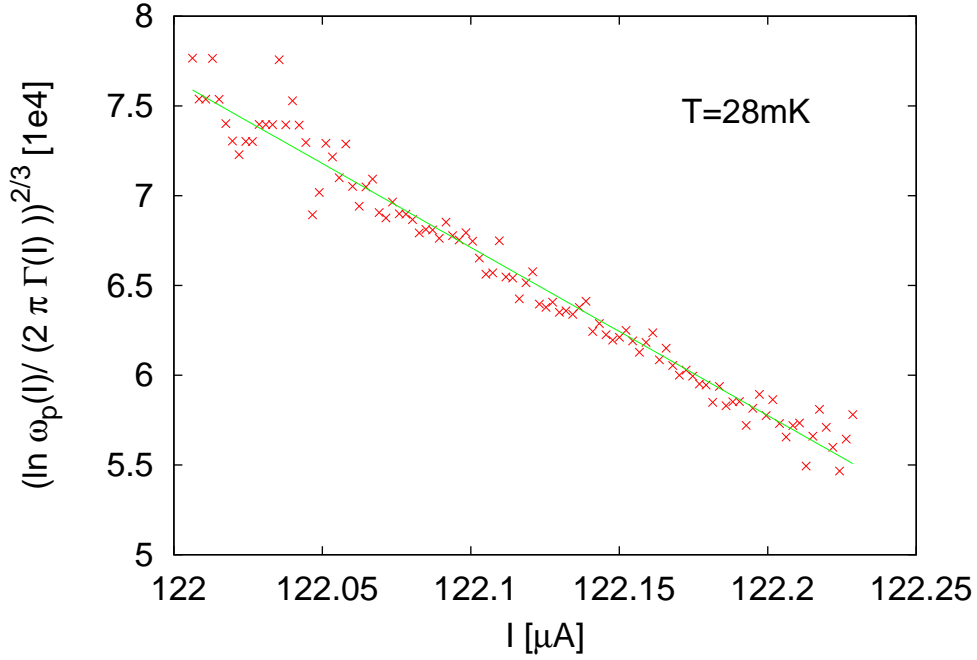


**Figure 5.8:** A plot of  $\left(\ln \frac{\omega_p}{2\pi\Gamma(I)}\right)^{2/3}$  vs.  $I_b$  for the data shown in fig. 5.5 and a linear fit for this data.

The green line with slope  $l$  denotes a least squares linear fit of the data. The fit crosses the abscissa at the critical current  $I_{c0}$ , which is obtained in the absence of fluctuations and MQT ( $122.8\mu\text{A}$  in fig. 5.8). The escape temperature for the data in fig. 5.8 can be evaluated to

$$T_{esc} = -\frac{E_J\sqrt{32}}{3k_B l^{3/2}} \approx 192 \pm 5 \text{ mK} \quad . \quad (5.3)$$

The escape rate measurements have been made for different bath temperatures. Figure 5.9 gives the dependence of the critical current  $I_{c0}$  on the bath temperature for two different values of the duty cycle. Figure 5.10 displays the dependence of the escape temperature on the bath temperature.

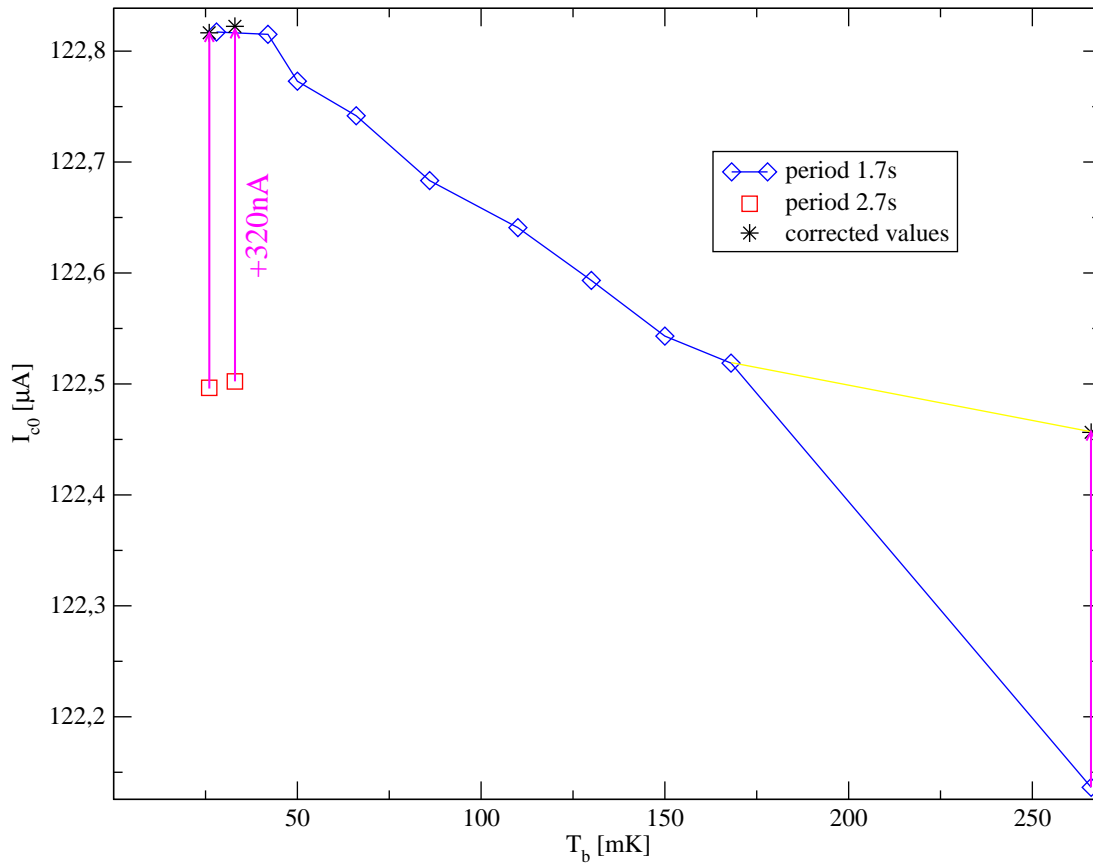


**Figure 5.9:** Critical current vs. bath temperature. The points displayed as diamonds have been measured first (except for the point at 270 mK) whereas the other points have been taken on the subsequent day. The significant offset (difference) at low temperatures may either be due to an incidental disadjustment of the offset of the sample and hold module or by different magnetic fields penetrating the junction. The arrows depict the effect for this offset by a translation.

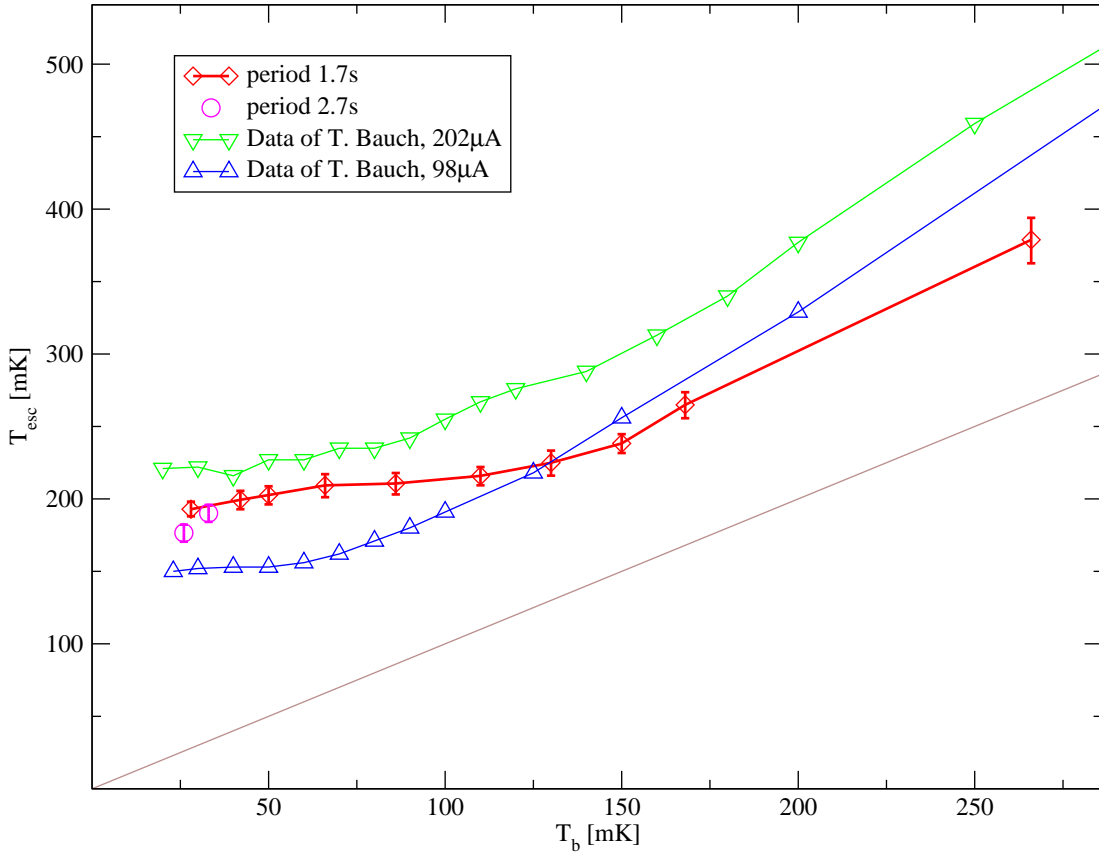


**Figure 5.10:** Escape temperature  $T_{esc}$  versus bath temperature  $T_b$  for different duty cycles. The green and blue line show results obtained by T. Bauch at Chalmers University, Sweden, for  $202 \mu\text{A}$  and  $98 \mu\text{A}$ , respectively. In these experiments the critical current was modified by applying a magnetic field.

Using the above described fitting procedure for fitting histograms is complicated especially for data taken at higher temperatures by several aspects. In the thermal regime the prefactor  $a_t$  (equation (2.11)) introduced in Büttiker's improvement to Kramers' theory (equation 2.10)<sup>5</sup> is not negligible for junctions with a high quality factor. Thus the escape temperature itself becomes current dependent. Furthermore, the low and high current limits of the histogram in the gamma values evaluated with equation (5.1) show considerable scatter, which might be related to the fact that only a few escape events are recorded for these channels. Therefore, this region has to be excluded from the fit. The errorbars in fig. 5.10 indicate the uncertainty calculated from the standard deviation of the fit. For the evaluation in fig. 5.10 I have tried to fit in a region such that a reasonable amount of data has been acquired for each channel and the scatter in the  $\Gamma$  values is not too big.

Nevertheless, there might be systematic errors. A bad choice of the fitting range and evaluating nearly empty channels may lead to deviations up to 10 mK or even more at higher temperatures. The parameters used for the evaluation like the junction capacitance, which was roughly estimated to 1 pF, and the rise time of the current ramp

only have minor influence. Figure 5.11 shows the escape temperature and the critical current vs. bath temperature of a measurement series where the critical current of the same Josephson junction was reduced to  $28 \mu\text{A}$  by accidentally trapping magnetic flux. In this measurements it was also tried to fit in the thermal limit (dashed lines).

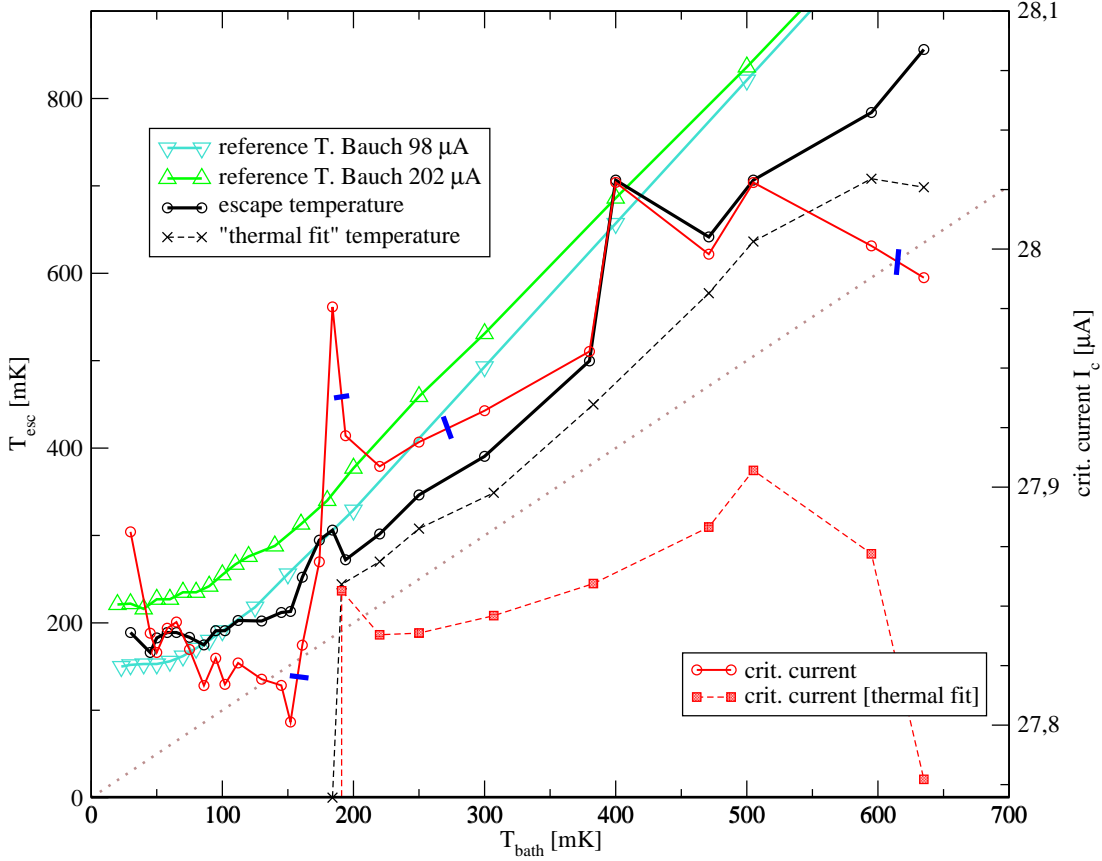


**Figure 5.11:** Escape temperature and critical current vs. bath temperature for the same junction as in fig. 5.10. Accidental trapping of magnetic flux led to a reduction of the critical current to  $28 \mu\text{A}$ . The blue lines indicate where the series was stopped overnight. For the measurements between 150 mK and 200 mK temperature instabilities were observed during the measurement. The dashed lines show the characteristic temperature and the critical current vs. bath temperature achieved in a fit for the thermal limit (equation (2.10)), where for the calculation of  $a_t$  (equation (2.11))  $\alpha = 1$ ,  $Q = 100$  and  $T = T_{bath}$  was used.

### 5.2.3 Discussion of results

In the measurements shown in figs. 5.9 and 5.10 the values for a 1.7 s period below 200 mK have been taken first, while the rest was acquired during the following day. The critical current values taken on the second day are lower than the others. This might be caused by an incidental change of the sample and hold offset trimmer resistance, or more likely by a change of the magnetic flux through the junction. The black stars in fig. 5.10 show the data of the second day offset by 320 nA, such that the results

for the lowest temperatures are the same for both duty cycles. The critical current  $I_{c0}$  at the highest temperature now seems too high indicating that either the critical current cannot be corrected by a simple translation or more changes of the critical current took place during the measurement. As explained later the fit process might be a source for too high critical current values in the thermal regime, too.

In the measurement where the critical current was suppressed to  $28 \mu\text{A}$  an unusual temperature dependence of the critical current was observed (see fig. 5.11). Up to  $160 \text{ mK}$  the critical current decreases as expected, for higher temperatures an overall tendency to increasing critical currents with increasing temperature is obvious. An explanation to this observation might be a rearrangement of trapped flux at higher temperatures due to the probe current and inaccuracy of the fit process as explained later.

The main results of this work are given by the red and the pink values in fig. 5.10 and by the black line in fig. 5.11. The kink observable in the black line can be explained by the observed unstable temperature during the measurements. The influence of the slightly changed critical current can be neglected. For both measurement series a transition from a temperature dependent to a temperature independent behavior below a certain crossover temperature is clearly observable. In the low temperature regime the junction behaves as a macroscopic quantum object (MQT). At higher temperatures in both measurements the escape temperature increases linearly as theoretically expected for the thermal limit. The crossover temperature of approximately  $150 \text{ mK}$  is higher than the one observed in T. Bauch's measurement. This indicates that even with a  $1.7 \text{ s}$  duty cycle the junction is either still not in thermal equilibrium or an ohmic resistance causes some heating during ramping up.

The problem of the heating of the junction as long as the junction stays in the voltage state could be investigated by varying the duty cycle. To achieve this the critical current detection electronics was modified in this work. Instead of immediately initiating a new ramping cycle after a down-sweep, the electronics now requires an external trigger pulse to start a new ramp. By means of this external pulse the duty cycle dependence could be investigated. It turned out that for duty cycles below  $1.7 \text{ s}$  heating is observable resulting in a decrease of the measured critical current values (see fig. 5.12). To achieve shorter measurement times, which is especially important at lowest temperatures where phononic heat conductivity extremely decreases due to its cubic temperature dependence, the thermal coupling of the junction has to be improved. Good starting points would be to use thicker copper wires for the powder filters and make further tests of the contact scheme with the spring contacts, the sputtered gold structures on the Si wafer, and the Al-wire bonding.

At the lowest bath temperatures the escape temperature lies between the values T. Bauch measured for  $98 \mu\text{A}$  and  $202 \mu\text{A}$ , respectively, and therefore perfectly coincides with the expectations. At higher temperatures my escape temperature results cross the  $98 \mu\text{A}$  curve. This is due to the fact that the escape temperature defined in equation (2.16) does not include a prefactor. But in the thermal limit the prefactor  $a_t$  (equation (2.11)) is not negligible in junctions with a high quality factor  $Q$  and highly dependent on the switching current. Thus, to discuss the results in the thermal limit, the equations

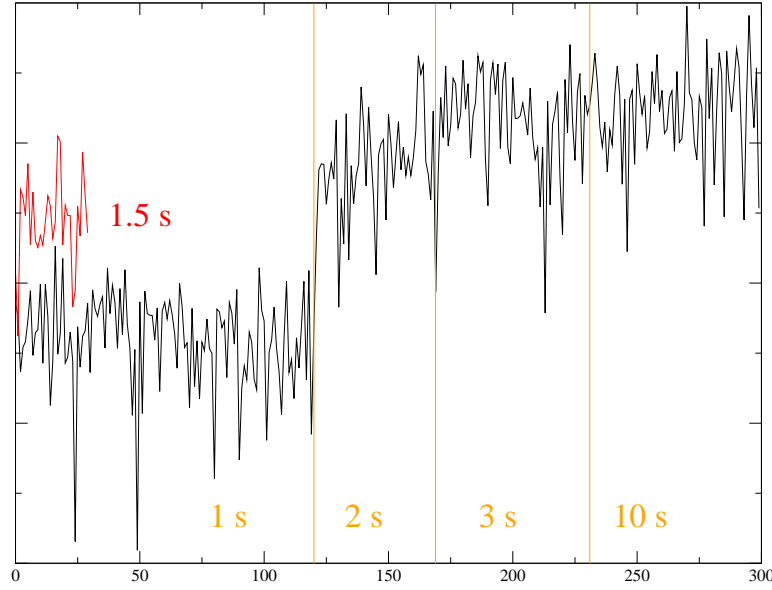


**Figure 5.12:** Switching current vs. measurement. With the technique described in section 5.2.1 switching currents have been measured whereby the length of the duty cycle has been varied. The measurement shows significant difference of the critical current for a duty cycle of 1 s, 1.5 s and 2 s while for longer duty cycles no change in the switching current is observed. This shows that the junction is not in thermal equilibrium during the measurements up to a duty cycle of about 2 s.

given by Büttiker and Kramers (equations (2.10) and (2.11)) have to be used.

The dashed lines in fig. 5.11 show a fit using this theory with the parameters  $\alpha = 1$ ,  $Q = 100$  and  $T = T_{bath}$ . The choice of this parameters seems to be of minor influence (although determining  $Q$  from critical and retrapping current is inexact for such high values and the temperature of the junction may deviate from the bath temperature). The values now obtained for the critical current are much lower than the values obtained in the fit to the escape temperature. Theoretically, this can be understood by looking at the maximum of a switching current histogram. The reduction of  $\Gamma$  leads on average to a lower distance between the switching currents and the critical current. Thus, if the less exact escape temperature equation is used in the fit, where the distance between switching currents and critical current is larger, the critical current is fitted to higher values. This rises the question whether the unusual temperature dependence of the critical current is really caused by a rearrangement of flux or whether we have to deal only with a fitting problem.

The values of the characteristic temperature  $T_t$ , as I will call the analog to the escape temperature in the thermal limit defined through equation (2.10), disagree with the theoretically expected values  $T_t = T_{bath}$ . This may be caused either by improper fit parameters or indicates that the junction still is not in equilibrium when the switching takes place.



Part IV

SUMMARY



In this work a low temperature setup to investigate superconducting flux qubits has been developed and extensively characterised. Successful measurements on Josephson junctions and flux qubits in the quantum regime require an experimental environment which is extremely well shielded from electromagnetic noise and radiation. Therefore, several stages of low-pass filters have been mounted at several temperature stages in a dilution unit. The final filtering setup described in section 4.4 turned out to be well suited to perform escape rate measurements on individual Josephson junctions. In these experiments a clear transition from a thermally activated temperature dependence at higher temperatures to a temperature independent regime at low temperatures where the junction escape is governed by MQT could be observed. From these results it can be judged that this setup should be well suited to experimentally investigate qubit structures. A bottleneck of the present experimental setup is excessive heating of the junctions. Although the critical currents in the flux qubit structures which are currently developed at the WMI are designed to be two orders of magnitude lower (resulting in a decrease of the dissipated heat by four orders of magnitude), thermal aspects will have to be closely inspected for future experiments. Despite this thermal problems it has been experimentally proved that environmental noise and radiation is not significant down to fractions of microamps.



## BIBLIOGRAPHY

- [1] V. Ambegaokar and A. Baratoff. Tunneling between superconductors. *Phys. Rev. Lett.*, 10(11):486–489, June 1963.
- [2] J. Bardeen, L. N. Cooper, and J. R. Schrieffer. Theory of superconductivity. *Phys. Rev.*, 108(5):1175–1204, December 1957.
- [3] K. Bladh, D. Gunnarsson, E. Hürfeld, S. Devi, C. Kristofferson, B. Smålander, S. Pehrson, T. Claeson, P. Delsing, and M. Taslakov. Comparison of cryogenic filters for use in single electronics experiments. *Rev. Sci. Inst.*, 74(3):1323–1327, March 2003.
- [4] P. E. Blöchl. Statistical physics. URL: [http://www.pt.tu-clausthal.de/atp/Scripts/sm\\_twopage.pdf](http://www.pt.tu-clausthal.de/atp/Scripts/sm_twopage.pdf), Downloaded: 07/26/2004, 2004.
- [5] M. Büttiker, E. P. Harris, and R. Landauer. Thermal activation in extremely underdamped Josephson-junction circuits. *Phys. Rev. B*, 28(3):1268, August 1983.
- [6] P. G. de Gennes. Boundary effects in superconductors. *Rev. Mod. Phys.*, 36:225–237, 1964.
- [7] M. Devoret and D. Esteve. Resonant activation of brownian particle out of a potential well: Microwave-enhanced escape from the zero voltage state of a Josephson junction. *Phys. Rev. B*, 36(1):58–73, July 1987.
- [8] D. P. DiVincenzo. The physical implementation of quantum computation. *arXiv:quant-ph 0002077*, April 2000. URL: <http://xxx.lanl.gov/pdf/quant-ph/0002077>.
- [9] D. Esteve, M. Devoret, and J. Martinis. Effect of an arbitrary dissipative circuit on the quantum energy levels and tunneling of a Josephson junction. *Phys. Rev. B*, 34(1):158–163, July 1986.
- [10] E. Freidkin, P. S. Riseborough, and P. Hänggi. Quantum tunneling at low temperatures: Results for weak damping. *Z. Phys. B*, 64:237–246, 1986. see also addendum, *Z. Phys. B*, 67:271, 1987.

- [11] A. Fukushima, A. Sato, A. Iwasa, Y. Nakamura, T. Kmatsuzaki, and Y. Sakamoto. Attenuation of microwave filters for single-electron tunneling experiments. *IEEE Trans. Instrum. Meas.*, 46(2):289, 1997.
- [12] T. A. Fulton and L. N. Dunkleberger. Lifetime of the zero-voltage state in Josephson tunnel junctions. *Phys. Rev. B*, 9(11):4760–4768, June 1974.
- [13] R. Gross and A. Marx. *Applied Superconductivity: Josephson Effect and Superconducting Electronics*. Walther-Meissner-Institut, Bayerische Akademie der Wissenschaften, 2004. (unpublished, older version available via <http://www.wmi.badw.de>).
- [14] L. Grover. *A fast quantum mechanical algorithm for database search*, pages 212–219. Proceedings of the 28<sup>th</sup> ACM Symposium on Theory of Computing. Association for Computing Machinery Press, New York, 1999.
- [15] P. Hänggi, P. Talkner, and M. Borkovec. Reaction-rate theory: fifty years after Kramers. *Rev. Mod. Phys.*, 62(2):251–341, April 1990.
- [16] B. D. Josephson. Possible new effects in superconductive tunnelling. *Physics Letters*, 1(7):251–253, July 1962.
- [17] H. Knoglinger. *Herstellung und Charakterisierung von Phasen-Qubits*. Walther-Meissner-Institut, Bayerische Akademie der Wissenschaften, Walther-Meissner-Str. 8, 85748 Garching, Germany, July 2004. Diploma Thesis.
- [18] H. A. Kramers. Brownian motion in a field of force and the diffusion model of chemical reactions. *Physica (Utrecht)*, 7:284–304, 1940.
- [19] R. Krücken and P. Ring. *Stabilität von Kernen*, chapter 3. Skript zur Vorlesung Kern- und Teilchenphysik 1. TU München, 2003. URL: <http://www.e12.physik.tu-muenchen.de/stud/vorlesungen/kruecken/kt1/Skript/3-Stabilitaet.pdf> Downloaded: 04/18/2004.
- [20] Ken Kundert. Power supply noise reduction, January 2004. URL: <http://www.designers-guide.com/Design/bypassing.pdf>.
- [21] K.K. Likharev. Superconducting weak links. *Rev. Mod. Phys.*, January 1979.
- [22] J. Lisenfeld. Probing quantum states of Josephson junctions by microwaves. Master’s thesis, Physikalisches Institut III, Friedrich-Alexander-Universität Erlangen-Nürnberg, February 2003.
- [23] Y. Makhlin, G. Schön, and A. Shnirman. Quantum-state engineering with Josephson-junction devices. *Rev. mod. phys.*, 73:357–400, April 2001.

- 
- [24] J. Martinis, M. Devoret, and J. Clarke. Energy-level quantization in the zero-voltage state of a current-biased Josephson junction. *Phys. Rev. Lett.*, 55(15):1543–1546, October 1985.
- [25] J. Martinis, M. Devoret, and J. Clarke. Experimental tests for the quantum behavior of macroscopic degree of freedom: The phase difference across a Josephson junction. *Phys. Rev. B*, 35(10):4682, April 1987.
- [26] D. E. McCumber. Effect of ac impedance on dc voltage-current characteristics of superconductor weak-link junctions. *Journal of Applied Physics*, 39:3113, 1968.
- [27] G. E. Moore. Cramming more components onto integrated circuits. *Electronics Magazine*, 38(8):114–117, April 1965. URL: <http://www.intel.com/research/silicon/moorespaper.pdf>.
- [28] T. P. Orlando, J. E. Mooij, L. Tian, C. H. van der Wal, L. S. Levitov, S. Lloyd, and J. J. Mazo. Superconducting persistent-current qubit. *Physical Review B*, 60(22):398–413, December 1999.
- [29] F. Schwabl. *Quantenmechanik*. Springer, 6. edition, 2002.
- [30] P.W. Shor. *Algorithms for quantum computation: discrete logarithms and factoring*, pages 124–134. Proceedings of the 35<sup>th</sup> Annual Symposium on the Foundations of Computer Science. S. Goldwasser, 1994.
- [31] T. P. Spiller. Superconducting circuits for quantum computing. *Fortschr. Phys.*, 48:1075–1094, 2000.
- [32] W. C. Stewart. Current-voltage characteristics of Josephson junctions. *Applied physics letters*, 12(8):277–280, April 1968.
- [33] Tinkham. *Introduction to superconductivity*. McGraw-Hill, New York, 1975.
- [34] K. Uhlig. Magnetoresistance of thick film chip resistors at millikelvin temperatures. *Cryogenics*, 35:525–528, 1995.
- [35] C. H. van der Wal, F. K. Wilhelm, C. J. P. M. Harmans, and J. E. Mooij. Engineering decoherence in Josephson persistent-current qubits. *Eur. Phys. J. B*, 31:111–124, 2003.
- [36] N.G. van Kampen. *Stochastic processes in physics and chemistry*. Elsevier Science publishers B.V., 1992.
- [37] L. M. K. Vandersypen, M. Steffen, G. Breyta, C. S. Yannoni, M. H. Sherwood, and I. L. Chuang. Experimental realization of shor’s quantum factoring algorithm using nuclear magnetic resonance. *Nature*, 414:883–886, December 2001.

- [38] C. J. M. Verwijs. Measurement of a flux qubit using the Josephson inductance of a dc squid. Master's thesis, Delft University of Technology, Faculty of Applied Sciences, Department of NanoScience, Quantum Transport Group, August 2003.
- [39] D. Vion, P. F. Orfila, P. Joyez, D. Esteve, and M. H. Devoret. Miniature electrical filters for single electron devices. *J. Appl. Phys.*, 77(6):2519–2524, March 1995.
- [40] P. Vogl. *Lecture Script on Advanced Quantum Mechanics, winter term 2001/02*, chapter 1–4. TU München, 2002.
- [41] A. Wallraff, A. Lukashenko, C. Coqui, T. Duty, and A. V. Ustinov. High resolution measurements of the switching current in a Josephson tunnel junction: Thermal activation and macroscopic quantum tunneling. *arXiv:cond-mat 0204527 v1*, April 2002. URL: <http://de.arxiv.org/pdf/cond-mat/0204527?>
- [42] A. Wallraff, A. Lukashenko, C. Coqui, A. Kemp, T. Duty, and A. V. Ustinov. Switching current measurements of large area Josephson tunnel junctions. *Rev. sci. inst.*, 74(8):3740–3748, August 2003.
- [43] Walther-Meissner-Institut, Bayerische Akademie der Wissenschaften, 85748 Garching. *Annual report*, 2002. URL: <http://www.wmi.badw.de/ueberuns/jahresberichte/2002.pdf>.
- [44] T. Zeeff, T. Hubing, T. van Doren, and D. Pommerenke. Analysis of simple two-capacitor low-pass filters. *IEEE Trans. Electrom. Compat.*, 45(4):595–601, November 2003.
- [45] Floris Zwanenburg. Superconducting electronics with phase biased squids. Master's thesis, Delft University of Technology, Department of NanoScience, Quantum Transport group, January 2003.